DANISH METEOROLOGICAL INSTITUTE

SCIENTIFIC REPORT

99-12

Simulations of current density measurements with a Faraday Current Meter and a Magnetometer

Hans-Henrik Benzon
Laust Olsen
Per Høeg

COPENHAGEN 1999

ISSN-Nr. 0905-3263
ISSN-Nr. 1399-1949 (Online)
ISBN-Nr. 87-7478-401-3

Abstract

The purpose of this report is to briefly summarize the present knowledge of field aligned current structures, densities and generation mechanisms and then to present the results of a computer simulation of direct current density measurements with a satellite borne Faraday Current Meter (FCM). The simulated FCM measurements are compared with both current densities estimated from simulated magnetometer measurements and model based current densities.

Nomenclature

σ_P	Pedersen conductivity
σ_H	Hall condutivity
$\vec{E}$	Electric field strenght
$\vec{D}$	Electric flux density
Ψ	Electric flux
$\vec{u}$	Velocity of particles in the sun wind
$\vec{H}$	Magnetic field strenght
$\vec{B}$	Magnetic flux density
B_x	X component of magnetic flux density
μ_0	Vacuum permeability
$\vec{j}$	Current density
$\vec{J}$	Current density
J_z	Z component of current density
Θ	Polarization angle of laser light
V	Verdet constant
$j_{\|\|}$	Current density parallel to the normal of the FCM plane
I	Total current
t	Time
x	Horizontal coordinate along satellite track
y	Horizontal coordinate normal to x and z
z	Vertical coordinate along background magnetic field
AlongYTubeNr	Y coordinate of the tube
OffSetFiber	Y coordinate of the FCM
xrc	X coordinate of tube center
μx	X coordinate of tube center
μy	Y coordinate of tube center
rc	Radius of the tube
Rp	Radius of the tube
rs	Radius of fiber loop
BigN[i,1]	Startpoint of i'th tube i.e BigN[i,2]−Rp
BigN[i,2]	X coordinate of the center of the i'th tube
BigN[i,3]	Endpoint of i'th tube i.e BigN[i,2]+Rp
BigN[i,4]	Endpoint of space between tubes i.e equal to BigN[i+1,1]
BigN[i,5]	Average current density
BigN[i,6]	Standardeviation of the current density in the i'th tube
BigN[i,7]	Mean current in the i'th tube
BigN[i,8]	Current direction (+1 (up) or −1(down))
FCM	Faraday Current Meter
MLT	Magnetic Local Time
IMF	Interplanetary Magnetic Field
PC	Polar Cap

Contents:

1.0 Introduction

In the ionosphere and magnetosphere electric currents are present. They are primarily directed parallel with the magnetic field lines as proposed by Birkeland in the start of the 20th century. Satellites have made it possible to measure the local magnetic field and particle precipitation and thereby estimate the local current densities. The magnetosphere structure is illustrated in figure 1.

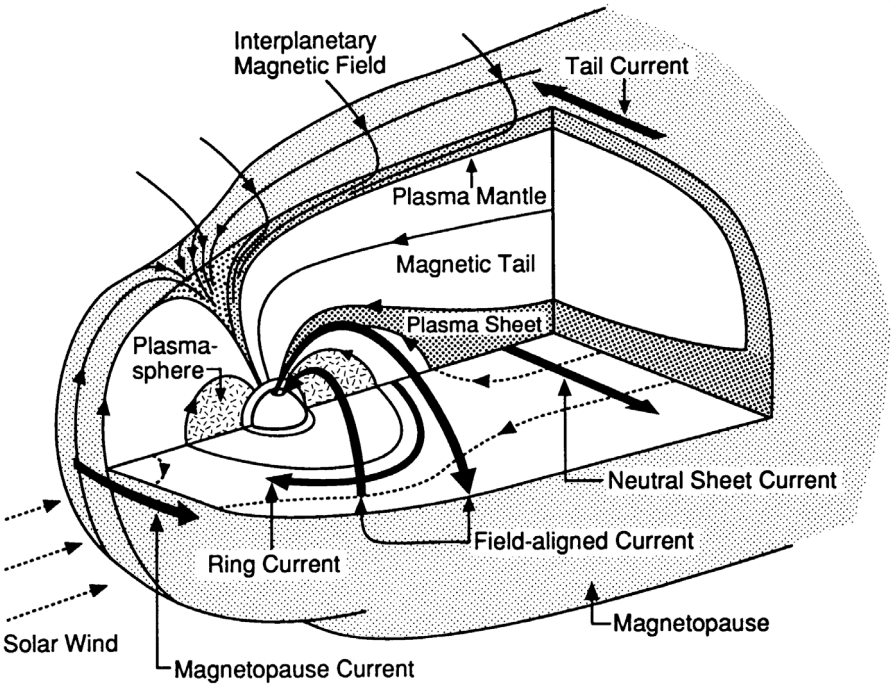

Fig 1. The structure of the magnetosphere. From *Kivelson and Russell* [1995].

Iijima and Potemra [1976] determined a large−scale mean current system in the high latitude ionosphere consisting of two current sheets parallel to the magnetic field, see figure 2. The sheets are centered at about 70 degrees geomagnetic latitude, ie where the magnetic field lines are almost radial, and are about 5 degrees wide.

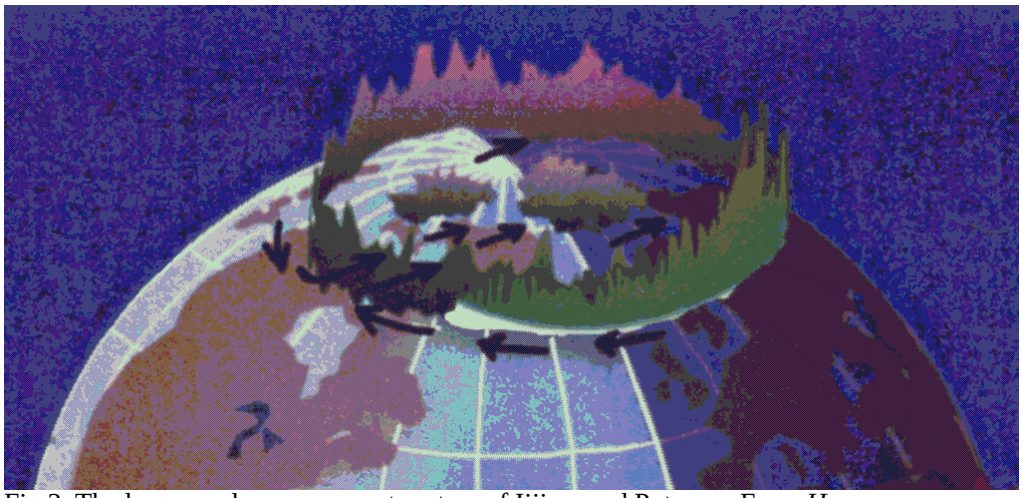

Fig 2. The large−scalemean current system of Iijima and Potemra. From *Hoeg* [1999].

The sheets are defined in a statistical way by the mean current density at the given magnetic latitude and Magnetic Local Time (MLT). The sheet near the pole is called region 1 and the sheet on the equatorial side is called region 2. At noon and midnight the pattern is irregular. Other large scale structures and deviations from the region 1 and 2 pattern has been found and described since. The current density in region 1 and 2 respectively is not homogen. The regions consist of smaller structures called filaments. It is not known how small the filaments might be or exactly what kind of physical processes that creates them. It is assumed that the structures might be as small as meter size, *Moretto and Olsen* [1998]. Neither the shape of the small structures are known. Maybe they are sheets like the large scale structures or maybe they are more like wires.

It should be noted that the region 1 and 2 pattern is based on statistics and is not necessarily the actual instantaneous current pattern. At a given time there might be an overall region 1 and 2 current system but the current in the filaments can vary greatly and even be oppositely directed within the same region. The current density in a filament is greater than the mean of the whole region. *Stasiewich and Potemra* [1998] find current densities of 100−300 μAmpere/m^2 in filaments of sizes less than 1 km at 1600 km altitude while *Olsen* [1999] find a mean current density for a whole region in the order of 0.01 μAmpere/m^2 at an altitude of 450 km

2.0 What drives the ionospheric currents

The following is a brief, and hopefully an intuitive understandable description rather than a physical precise, description of the ionospheric currents.

The ionosphere consists of a quasineutral plasma, ie a rarefied ionized gas with almost equal amounts of positive and negative charges. The conductivity in such a plasma in the presence of a magnetic field is anisotropic. In the ionosphere, the conductivity parallel to the magnetic field, is typical 10^6 times greater than the trans-

verse conductivities σ_P and σ_H at 450 km altitude. But in the lower parts (under 150 km) the difference is much less.

The solar wind is a radial flow of particles ejected from the sun. In the solar wind as well as in the Earths magnetosphere the magnetic Reynold number is sufficiently high, while the conductivity is high, that the "frozen−in"condition is satisfied. Frozen−in implies that two plasma particles initially on the same magnetic field line stays on a common field line. Particle flow and deformation of the magnetic field are therefore closely related. A consequence of the frozen−in condition is that the interplanetary plasma and the magnetospheric plasma is sharply separated.

If the Interplanetary Magnetic Field (IMF) is antiparallel with, or just have a component opposite to the earths magnetic field at the nose of the magnetosphere, "reconnection" can take place. Reconnection is when the frozen−in conditions locally breaks down and magnetic field lines and the plasma on these mix. Only the outermost field lines of the earths dipolelike magnetic field reconnect, ie those originating from the polar regions (polar cap, PC). The solar wind still drags the part of the field line that is in the interplanetary space and therefore the field line moves as shown in figure 3.

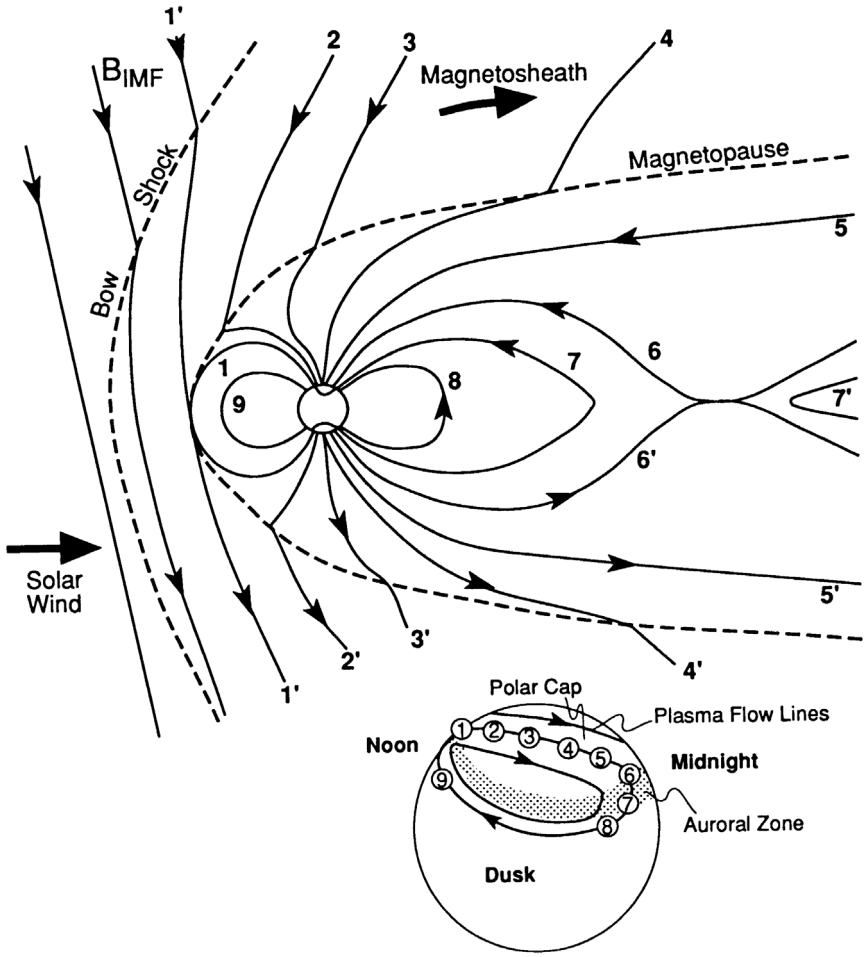

Fig 3. Reconnection happens where the IMF field line 1' and the Earths field line 1 meets. As time goes by the reconnected field lines are dragged by the solar wind and frozen−incondition to positions 2,3,... and 2',3',... . From *Kivelson and Russell* [1995].

Outside the relatively small reconnection area at the nose of the magnetosphere the frozen−in condition rules again. When the conductivity is very high, the general Ohms law reduces to $\vec{E}=-\vec{u}\times\vec{B}$ where u is the velocity of the charged particles, E are the electric field and B are the magnetic field. From this it is evident that the solar wind and the IMF induces an electric field unless they are parallel. This electric field in the interplanetary space causes a potential difference over the magnetosphere as shown in figure 4, which is taken from *Akasofu* [1989]. Because of the frozen−in condition, i.e almost infinite conductrivity, magnetic field lines are (almost) equipotential lines and the potential difference at the magnetopause maps down to the ionosphere in the polar cap (PC) where the reconnected field lines is "attached". The potential difference is about 100.000 Volts *Akasofu* [1989]. The potential difference drive currents across the magnetosphere and in the ionosphere across the polar cap, also shown in figure 4. Since the potential difference is maintained by the solar wind these currents are forced to go on. This is not possible unless the current carriers (electrons) are returned somehow. *Akasofu* [1989] arguments that the total current system end up as shown in figure 4. The currents between the magnetopause and the ionosphere is supposed to be the region 1 currents.

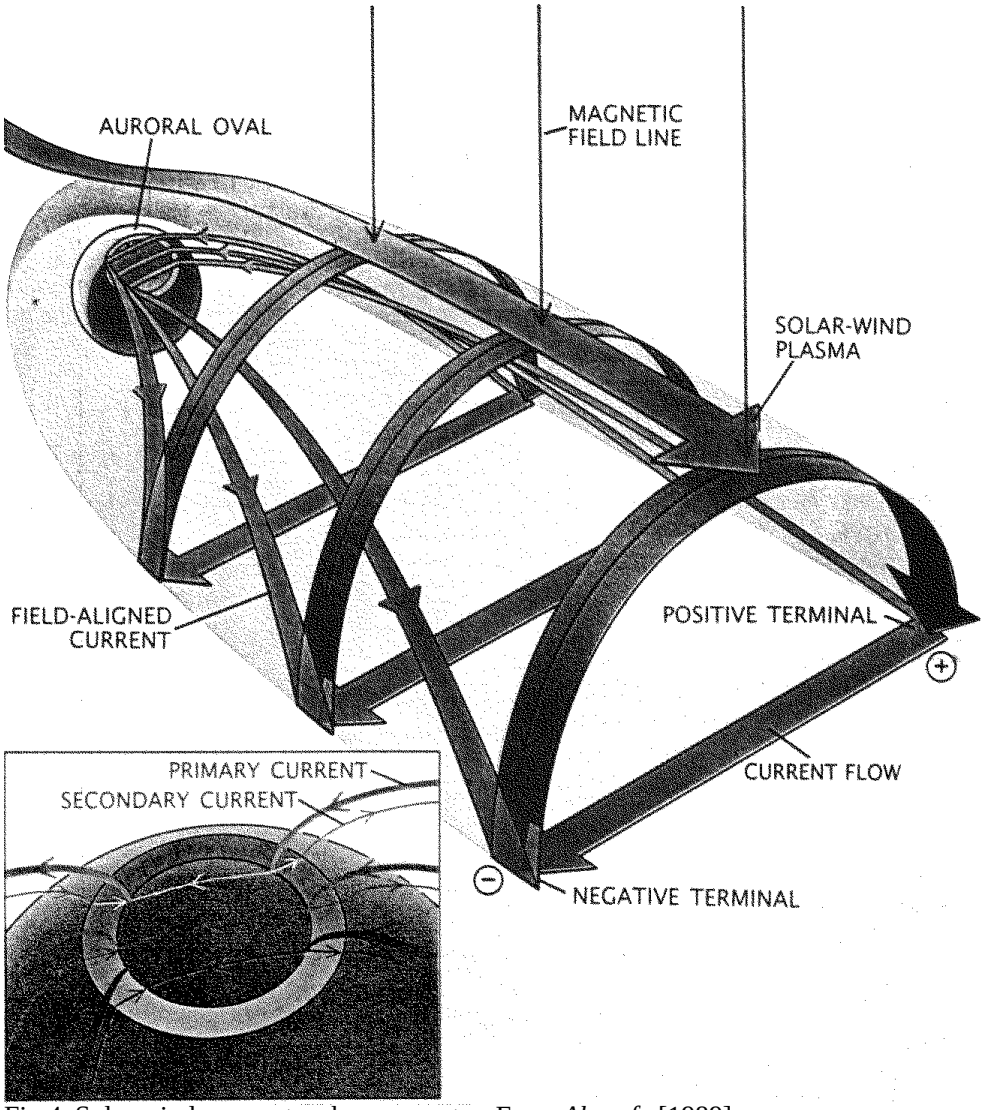

Fig 4. Solar wind−magnetospheregenerator. From *Akasofu* [1989].

Mechanisms not entirely known generates secondary currents which is the region 2 currents described above.

3.0 Different satellite based techniques to measure the current densities

The following sections contain a discussion of the techniques that can be used to measure the current densities in the ionosphere and magnetosphere. This discussion is followed by a simulation studie where the responses of two satellite borne instruments, the magnetometer and the Faraday Current Meter, are simulated using a 20 "tube" current structure model.

3.1 Magnetometer

A satellite borne magnetometer measure the three components of the total magnetic field at different places at the satellite orbit. To derive a local current density from these data, one have to subtract the part of the field not caused by the local current

density. But then you have to know the local current density. Assumptions and simplifications have to be made. The Earths magnetic field (a spherical harmonic function model) must first be subtracted from the measured field to get the residual field. From now on the residual magnetic field is just called the magnetic field. Next we assume that the current structures in the ionosphere can be approximated by sheets and the currents are parallel to the earths magnetic field as described earlier. If the satellite cross the sheets at right angles Amperes law for steady state

$$\nabla \times \overline{B} = \mu_0 \overline{J} \qquad (1)$$

reduces to

$$J_z = \frac{1}{\mu_0} \frac{B_x}{\mathrm{d}y} \qquad (2)$$

in a coordinate system with z axes along the background magnetic field (the subtracted Earth field model), y−axie along the satellite velocity vector and the x−axes makes the system orthogonal and right handed. Among others *Lühr et al* [1996] has used these assumptions and has carried out model simulations for an almost infinitely large 1 km thick current sheet with constant current density and a satellite with a velocity of 8 km/s and a magnetometer sampling rate of 8 s^{-1}. The estimated current density in the sheet was 9% less than the actual. Outside the sheet it is only in the near vicinity of the sheet the model erroneously claims a small current density. It should be kept in mind that such a model is highly idealized and never occur in reality and the points of measurement is also placed favorably.

3.2 Faraday Current Meter (FCM)

The Faraday Current Meter (FCM) consist of a light source emitting linearly polarized laser light, a circular loop of optical fiber and a detector which measure the polarization of the received laser light. A detailed description of the FCM instrument can be found in "A New Method for Measuring Space Plasma Current Densities by the Faraday Rotation of Laser Light in Optical Monomode Fibers" (DSRI, 1986). Linearly polarized light in a dielectricum exposed to a magnetic field parallel to the direction of propagation (of the light) will change the polarization angle of the laser light. The polarization plane is rotated an angle

$$\theta = \mathrm{V} \int_L \overline{H} \cdot d\,\overline{l} \qquad (3)$$

where V is the Verdet constant for the fiber, L is the total length of the fiber ($L = 2\pi Rn$, where n is the number of windings, R the radius of the fiber loop) and $\overline{H}$ is the magnetic field strength. Through Amperes law

$$\int_L \overline{H} \cdot d\,\overline{l} = \int_S \overline{j} \cdot d\,\overline{a} \qquad (4)$$

and some rewriting one obtains, for a circular fiber loop

$$\theta = 1/2VRL j_{\perp} \qquad (5)$$

$\bar{j}$ is the total current density through the loop, while $j_{\perp}$ is the current density normal to the plane of the fiber loop. The two major advantages of the FCM method compared to the magnetometer method are

1. The FCM method do not depend on a geometric assumption for the current distributions

2. The method it is not influenced by neighbor/remote currents.

Two following two limitations of the FCM instrument have to be taken into account

1. The fiber loop has to be greater than the electron gyroradius if not to be influenced by single particle motions.

2. Current structures of smaller scale than the fiber loop cannot be detected.

The last limitation is due to the fact that the measured change in the polarization angle is proportional to the total current through the fiber loop, see equation 4 and 5.

4.0 Model and Simulations

In order to compare the responses of the FCM and the magnetometer, a very simplified model of the ionosphere and magnetosphere was assumed. This very simplified model consist of a number of infinitely long cylinder shaped current filaments (tubes). It is assumed that contributions from currents outside this region can be neglected. The measurements performed by a FCM and a magnetometer placed on a satellite that traverses the model of the ionosphere/magnetosphere are simulated. The simulated FCM and magnetometer current density measurements can after the simulation be compared to the current densities intrinsic to the model. The current density distribution in the tubes are Gaussian and the current density falls almost off to zero at the edges of the tubes. The value of the standard deviation is selected in such a way that the width of the distribution is comparable to the size of the tube. The sizes of the tubes, distances between tubes and current directions (up/down) etc. are randomly chosen within intervals set by the maximum and minimum values of the parameters. The model and the simulations have been implemented in *Mathematica.* This gives a high degree of flexibility. A listing of the *Mathematica* code that implements the model and the instrument simulations can be found in the appendices.

The setup parameters for the model and instrument simulations corresponding to the figures found below are

Total number of current tubes 20

Maximum diameter of tube 110 meter
Minimum diameter of tube 50 meter
Maximum spacing between tubes 100 meter
Minimum spacing between tubes 50 meter
Maximum value of the current density in a tube 200 $\frac{\mu A}{m^2}$
Minimum value of the current density in a tube 10 $\frac{\mu A}{m^2}$
Sampling frequency of the instruments 2000 Hz
Satellite velocity 7000 m/s
Diameter of the FCM optical fiber loop 10 meter

The position and size in a horizontal cross section (x−y plane) of the cylinder shaped current tubes of the model can be seen in figure 5 for the particular simulation run. The tubes in the model are infinitely long in the z direction. Figure 6 illustrates the corresponding current density distributions in the 20 tubes. The sign indicates the current direction and the current density is assumed to be zero between the pipes.

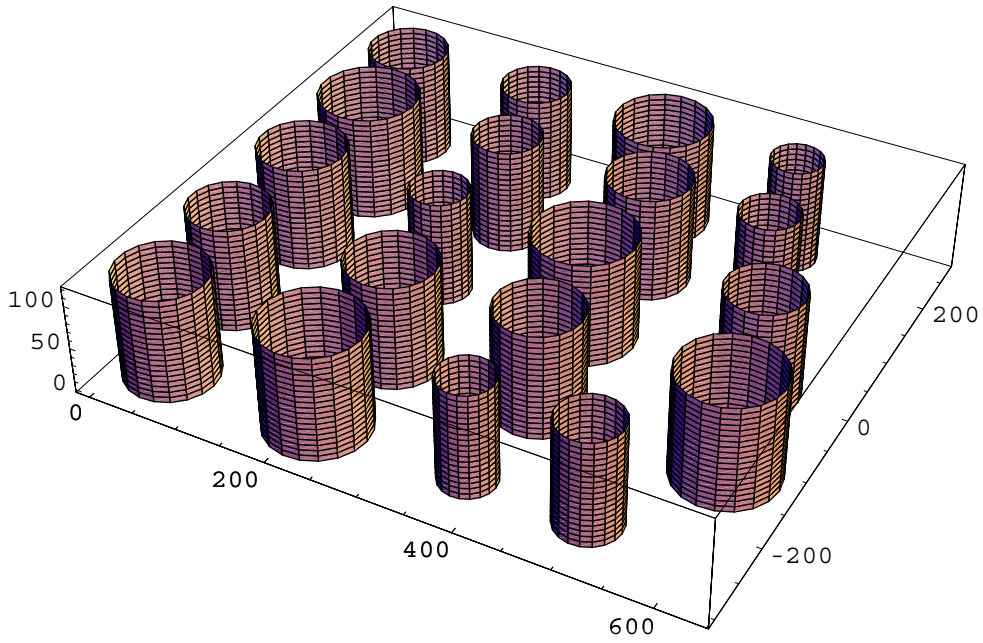

Fig 5. Position and size of the 20 cylinder shaped current tupes. The values on the x,y and z−axesare measured in units of meters.

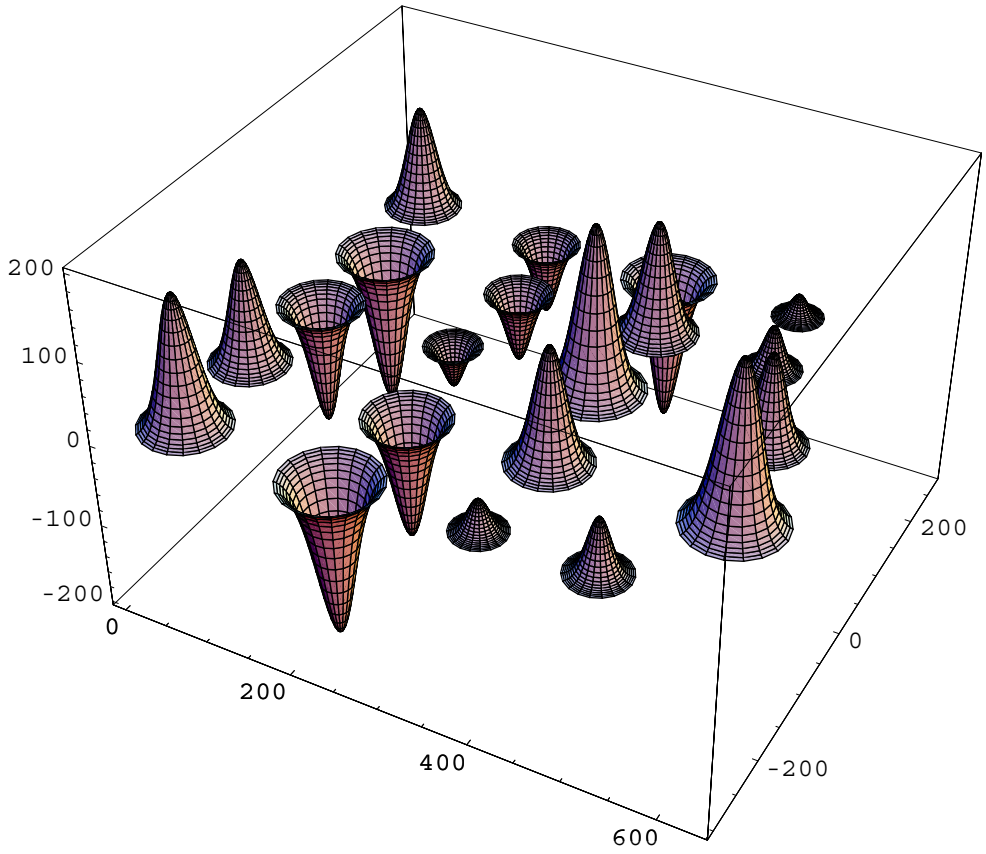

Fig 6. The figure shows the Gaussian current density distribution in the 20 tubes of the model. The values on the x and y axes are measured in meters, the unit for the z−axesis μA/m^2.

Three methods was used to calculate the magnetic field. It is necessary to calculate the magnetic field in order to determine the response of the magnetometer. The measured current density is proportional to the derivative of one of the components of the magnetic field, see the description of the magnetometer. The three methods are discussed below.

The basic tool is Amperes law on either differential or integral form:

$$\nabla \times \overline{H} = \overline{J} + \frac{\partial \overline{D}}{\partial t} \quad (6)$$

and

$$\oint_C \overline{H} \cdot d\overline{l} = \mathrm{I} + \frac{d\Psi}{d\mathrm{t}} \quad (7)$$

It can be shown that the time derivatives can be neglected in field aligned currents in the ionosphere, *Holmegaard* [1998]. The equations then reduces to

$$\nabla \times \overline{H} = \overline{J} \quad (8)$$

and

$$\oint_C \overline{H} \cdot d\overline{l} = \mathrm{I} \qquad (9)$$

In method 1 and 2 it is used that the z component of the magnetic field is zero because the currents are all in the z direction and extends to infinity.

4.1 Method 1

If Amperes law on integral form is applied to one of the tubes with a Gaussian current density distribution, it is possible to calculate the corresponding magnetic field. The magnetic field is tangential to concentric circles around the center of the tube. Under the assumption of a current density of the form

$$\mathrm{GausCurrent}[x, \sigma, \mathrm{mn}] = \mathrm{mn}\, e^{-(x)/(2\sigma^2)} \qquad (10)$$

the magnetic field is given by

$$\mathrm{ModelH}(x, \sigma, \mathrm{mn}, \mathrm{rc}) = \begin{cases} \dfrac{+\left(1 - e^{-\frac{x^2}{2\sigma^2}}\right)\mathrm{mn}\,\sigma^2}{x} & \text{for } |x| \le \mathrm{rc} \\ \dfrac{+\left(1 - e^{-\frac{\mathrm{rc}^2}{2\sigma^2}}\right)\mathrm{mn}\,\sigma^2}{x} & \text{for } |x| > \mathrm{rc} \end{cases} \qquad (11)$$

where mn and σ is the maximum current density and the standard deviation while rc, x is the radius of the cylinder and the distance from the center of the cylinder to the point of observation. Figure 7 shows the variations in the magnetic field corresponding to a Gaussian current density distribution. Due to the principle of superposition the total magnetic field strenght in a given point, can simply be found by adding the vector fields of all 20 tubes. The total vector field is given by the following equation

$$\begin{aligned} &\mathrm{VecModelH}(x, y) = \\ &\sum_{i=1}^{\mathrm{TotalPipes}} \mathrm{ModelH}\left(\sqrt{(y - \mathrm{AlongY}[i])^2 + (x - \mathrm{BigN}[i, 2])^2}, \sigma[i], \mathrm{mn}[i], r[i]\right) \\ &\quad \{-\sin(\tan^{-1}(x - \mathrm{BigN}[i, 2], y - \mathrm{AlongY}[i])), \\ &\quad\ \cos(\tan^{-1}(x - \mathrm{BigN}[i, 2], y - \mathrm{AlongY}[i])), 0\} \end{aligned} \qquad (12)$$

mn, σ, AlongY, BigN are all arrays with a size equal to the total number of tubes. AlongY and r give us the y coordinate and the radius of the tube respectivly. The magnetic field x and y components, as a function of x, can now be given as

$$\begin{aligned} &\mathrm{CompXVecModelH}[x, y] = \\ &\sum_{i=1}^{\mathrm{TotalPipesModelH}} \left(\sqrt{(y - \mathrm{AlongY}[i])^2 + (x - \mathrm{BigN}[i, 2])^2}, \sigma[i], \mathrm{mn}[i], r[i]\right) \{-\sin(\tan^{-1}(x - \mathrm{BigN}[i, 2], y - \mathrm{AlongY}[i]))\} \end{aligned} \qquad (13)$$

$$\begin{aligned} &\mathrm{CompYVecModelH}[x, y] = \\ &\sum_{i=1}^{\mathrm{TotalPipesModelH}} \left(\sqrt{(y - \mathrm{AlongY}[i])^2 + (x - \mathrm{BigN}[i, 2])^2}, \sigma[i], \mathrm{mn}[i], r[i]\right) \{\cos(\tan^{-1}(x - \mathrm{BigN}[i, 2], y - \mathrm{AlongY}[i]))\} \end{aligned} \qquad (14)$$

It will in general not be possible to obtain an explicit expression for the magnetic field from a known current density distribution. The magnetic field can in these cases be calculated using method 2 and 3.

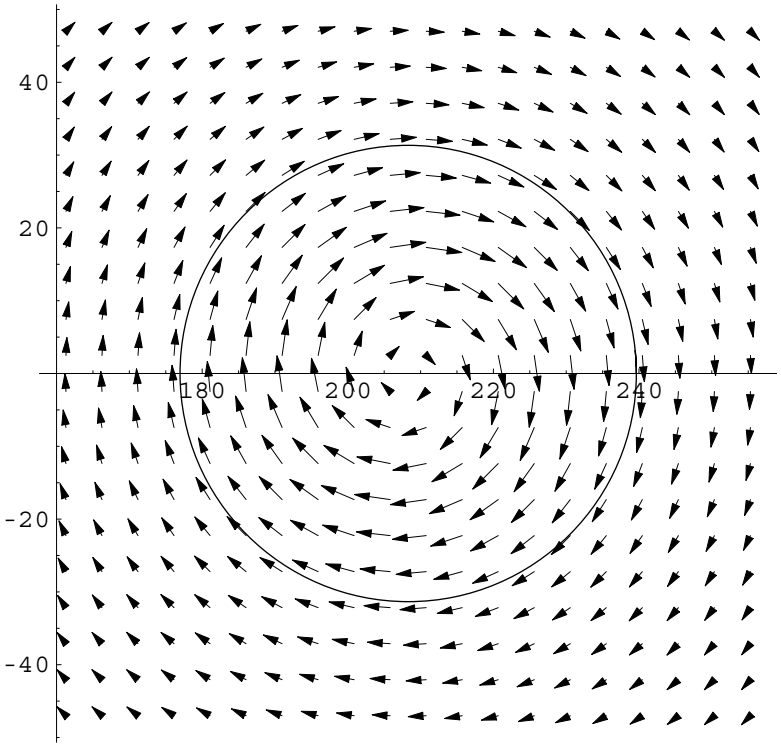

Fig 7. Magnetic field inside and outside a tube for a Gaussian current density distribution.

4.2 Method 2

The tubes are assumed to consist of an infinitely number of infinitely thin and infinitely long wires, each wire with a current given by its current density multiplied by the infinitesimal area it occupies in the x−y plane. The magnetic field will, for a cylindrical shape of the pipes, be tangential to concentric circles around the wires and only depend on the radial distance r from the center of the wire. The magnetic field around one of the wires are known to be given by

$$H=\frac{I}{2\pi r} \qquad (15)$$

where I is the current in the wire. The equation above give us the magnetic field in a cylinder coordinate system placed in the center of the wire. When this field is expressed in a Cartesian coordinate system that has its center in the middle of a tube, each wire will then have magnetic field components along the x and y−axes.These components can be found from geometric considerations. The magnetic field for a tube can hereafter be found by integration of the x and y field components separately. This vector field is given by the following formula

(16)

HphiXAndYCom[t, μy, σ, mn, rc, μx] =

$$\int_0^{2\pi}\int_0^{\text{rc}} \frac{1}{2\pi}\left\{\frac{\text{GausCurrent}[(\text{r Cos}[\theta])^2+(\text{r Sin}[\theta])^2,\sigma,\text{mn}]\ \text{r}}{\sqrt{(\text{Globalx}-\mu\text{x}-\text{r Cos}[\theta])^2+(\text{v t}-\mu\text{y}-\text{r Sin}[\theta])^2}}\right.$$
$$\frac{\text{v t}-\mu\text{y}-\text{r Sin}[\theta]}{\sqrt{(\text{Globalx}-\mu\text{x}-\text{r Cos}[\theta])^2+(\text{v t}-\mu\text{y}-\text{r Sin}[\theta])^2}},$$
$$\frac{\text{GausCurrent}[(\text{r Cos}[\theta])^2+(\text{r Sin}[\theta])^2,\sigma,\text{mn}]\ \text{r}}{\sqrt{(\text{Globalx}-\mu\text{x}-\text{r Cos}[\theta])^2+(\text{v t}-\mu\text{y}-\text{r Sin}[\theta])^2}}$$
$$\left.\frac{\text{Globalx}-\mu\text{x}-\text{r Cos}[\theta]}{\sqrt{(\text{Globalx}-\mu\text{x}-\text{r Cos}[\theta])^2+(\text{v t}-\mu\text{y}-\text{r Sin}[\theta])^2}}\right\} d\,\text{r}\,d\theta$$

The parameters in the equation are given by

Globalx: vertical distance between the satellite trajectory and x−axes
t: time
μy: position along the x−axes of the tube center
σ: standard deviations of the current density
mn: maximum current density
rc: radius of the tube
μx: position along the y−axis of the tube center

The integrals in the equation use a cylinder coordinate system placed in the center of the tube. This gives us simpler limits on the integrals. The total field is found by adding the magnetic vector fields from all of the tubes in the model. This method can be used to find the response of a magnetometer where the expression for the magnetic field can not be given in an explicit formula.

4.3 Method 3

Biot and Savarts law

$$\overline{B}(\overline{R})=\frac{\mu_0}{4\pi}\int_V \frac{\overline{J}(\overline{r})\times(\overline{R}-\overline{r})}{(|\overline{R}-\overline{r}|)^3}\,dv \qquad (17)$$

is used in this method. This law tell us that the field in the point $\overline{R}$ can be found by integrating the term $\frac{\overline{J}(\overline{r})\times(\overline{R}-\overline{r})}{(|\overline{R}-\overline{r}|)^3}$ over a volume V (here the tubes). The current density $\overline{J}$ must be known in this volume. This approach is similar to what is done in the Fresnel diffraction theory. Instead of assuming infinitely long pipes they were set to extent from −700km(=a) to 700 km(=b) in the z direction. Using this law one finds that one of the magnetic field components (the component perpendicular to the trajectory of the satellite) as a function of the satellite position x=vt is given by

$$\text{HfieldXCom}[t, \mu, \sigma, mn, y, rc, a, b] =$$

$$1/(4\pi)\int_0^{2\pi}\int_0^{rc} Rr\, E^{-\frac{Rr^2}{2\sigma^2}}\, mn\,(-y+\mu+Rr\,\text{Sin}[\text{Ttheta}])$$

$$\left(-\left((a-z)\left(1+\frac{(a-z)^2}{(\text{Globalx}-Rr\,\text{Cos}[\text{Ttheta}])^2+(-y+\mu+Rr\,\text{Sin}[\text{Ttheta}])^2}\right)^{1.5`}\right)\right.$$

$$\left(((a-z)^2+(\text{Globalx}-Rr\,\text{Cos}[\text{Ttheta}])^2+(-y+\mu+Rr\,\text{Sin}[\text{Ttheta}])^2)\text{\^{}}1.5`\right.$$

$$\left.\left(1+\frac{1.`\,(a-z)^2}{(\text{Globalx}-1.`\,Rr\,\text{Cos}[\text{Ttheta}])^2+(y-1.`\,(\mu+Rr\,\text{Sin}[\text{Ttheta}]))^2}\right)\text{\^{}}0.5`\right)+$$

$$\left((b-z)\left(1+\frac{(b-z)^2}{(\text{Globalx}-Rr\,\text{Cos}[\text{Ttheta}])^2+(-y+\mu+Rr\,\text{Sin}[\text{Ttheta}])^2}\right)^{1.5`}\right)\Big/$$

$$\left(((b-z)^2+(\text{Globalx}-Rr\,\text{Cos}[\text{Ttheta}])^2+(-y+\mu+Rr\,\text{Sin}[\text{Ttheta}])^2)^{1.5`}\right.$$

$$\left.\left.\left(1+\frac{1.`\,(b-z)^2}{(\text{Globalx}-1.`\,Rr\,\text{Cos}[\text{Ttheta}])^2+(y-1.`\,(\mu+Rr\,\text{Sin}[\text{Ttheta}]))^2}\right)\text{\^{}}0.5`\right)\right)dRr\,d\text{Ttheta}$$

(18)

Method 1 is the simplest method. It is derived from the general laws simplified by the cylindrical symmetry and the integration can for a Gaussian current density be performed symbolic. The method therefore required the shortest computation time. All three methods yielded the same results. The following plot shows the sum of the magnetic fields in the x−y plane from the 20 tubes indicated in the figure. The plot is calculated with the use of equation (12).

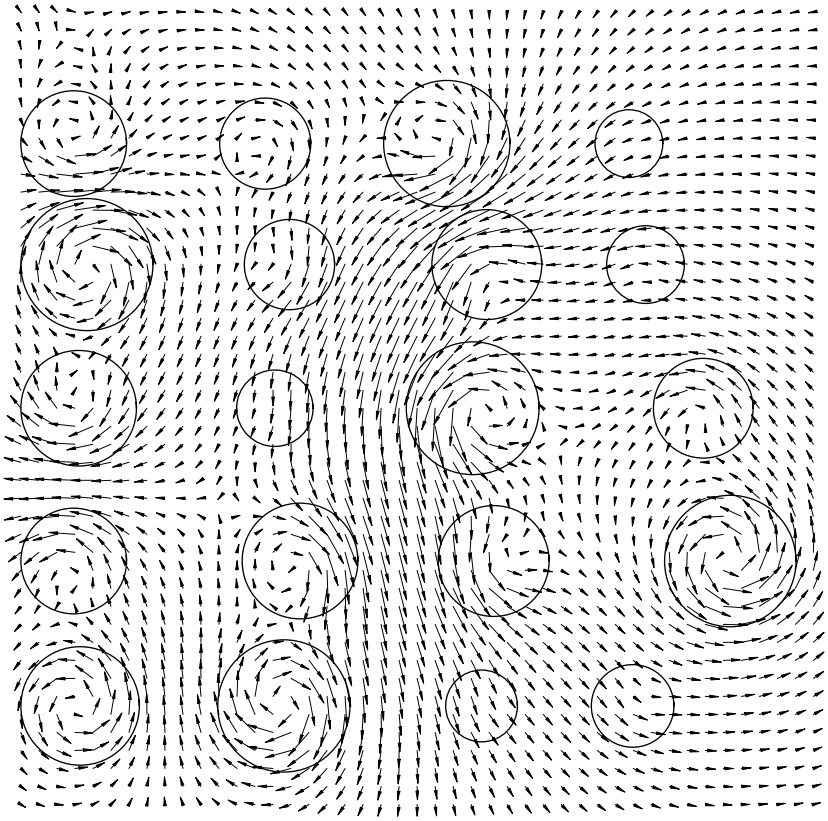

Fig 8. Total magnetic field around the 20 tubes used in the simulation.

4.4 FCM response

Figure 9 shows a simulation setup where the distance between the satellite trajectory and the global x−axes is 100 meter. It has been showed above that the current density response for the FCM can be calculated as the total current through the fiber optical loop divided by the area in which the current flow. This gives 3 different simulation cases.

1. The optical fiber loop is placed entirely in a current cylinder.

2. The optical fiber loop is on the boundary of a current cylinder.

3. The optical fiber loop is placed between two current cylinders. The current density response will in this case be 0.

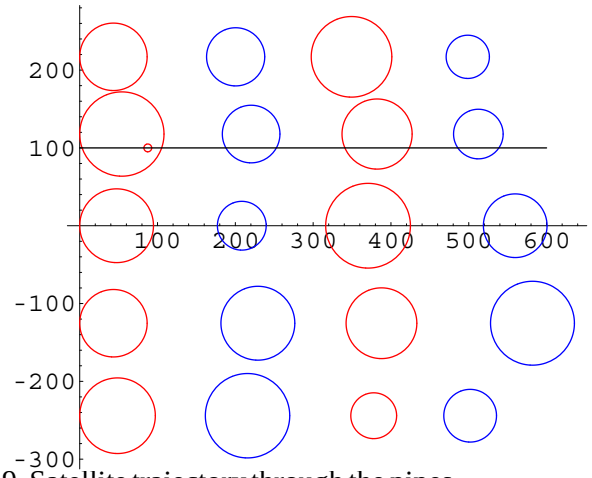

Fig 9. Satellite trajectory through the pipes.

The FCM response in the first two cases can be expressed by the rather long expressions given below

$$\text{FCMJCase1}(t, \mu, \sigma, \text{mn}, \text{AlongYTubeNr}, \text{xrc}) = \frac{1}{\pi\, r_s{}^2} \int_0^{rs} \int_0^{2\pi} \text{GausCurrent}\Big(\Big(r\cos(\theta) - \sqrt{(\text{AlongYTubeNr} - \text{OffSetFiber})^2 + (\text{xrc} - v\,t)^2} \Big)^2 + (r\sin(\theta))^2, \sigma, \text{mn} \Big)\, r\, d\theta\, dr \quad (19)$$

$$\text{FCMJCase2}(t, \mu, \sigma, \text{mn}, \text{xrc}, \text{Rp}, \text{AlongYTubeNr}) = \frac{1}{\text{Asb1}()} \Bigg(2 \int_{\frac{|\text{XCross}(\text{xrc},t,\text{Rp},\text{AlongYTubeNr})|}{\cos(\theta)}}^{\text{Rp}} \int_0^{\frac{1}{2}\theta p(\text{xrc},t,\text{Rp},\text{AlongYTubeNr})} \text{GausCurrent}(r^2, \sigma, \text{mn})\, r\, d\theta$$

$$
\begin{aligned}
&\partial r + \text{Which}\Big[\,|v\,t| > |xrc - |XCross\,(xrc,\,t,\,Rp,\,AlongYTubeNr)|| \wedge \\
&\quad |v\,t| < |xrc + |XCross\,(xrc,\,t,\,Rp,\,AlongYTubeNr)||, \\
&2\int_0^{rs}\int_0^{\pi-\frac{1}{2}\,\theta s\,(xrc,t,Rp,AlongYTubeNr)} \text{GausCurrent}\Big(\Big(r\cos(\theta) - \\
&\qquad \sqrt{(AlongYTubeNr - OffSetFiber)^2 + (xrc - v\,t)^2}\,\Big) \wedge \\
&\qquad 2 + (r\sin(\theta))^2,\,\sigma,\,mn\Big)\,r\,\partial\theta\,\partial r + \\
&2\int_0^{\frac{\left|\,|XCross\,(xrc,t,Rp,AlongYTubeNr)| - \sqrt{(AlongYTubeNr-OffSetFiber)^2+(xrc-v\,t)^2}\,\right|}{\cos(\theta)}} \\
&\qquad \int_0^{\frac{1}{2}\,\theta s\,(xrc,t,Rp,AlongYTubeNr)} \text{GausCurrent}\Big(\Big(r\cos(\theta) - \\
&\qquad\qquad \sqrt{(AlongYTubeNr - OffSetFiber)^2 + (xrc - v\,t)^2}\,\Big) \wedge \\
&\qquad\qquad 2 + (r\sin(\theta))^2,\,\sigma,\,mn\Big)\,r\,\partial\theta\,\partial r, \\
&|v\,t| \le |xrc - |XCross\,(xrc,\,t,\,Rp,\,AlongYTubeNr)|| \vee \\
&\quad |v\,t| \ge |xrc + |XCross\,(xrc,\,t,\,Rp,\,AlongYTubeNr)||, \\
&2\int_{\frac{\left|\,|XCross\,(xrc,t,Rp,AlongYTubeNr)| - \sqrt{(AlongYTubeNr-OffSetFiber)^2+(xrc-v\,t)^2}\,\right|}{\cos(\theta)}}^{rs} \\
&\qquad \int_0^{\frac{1}{2}\,\theta s\,(xrc,t,Rp,AlongYTubeNr)} \text{GausCurrent}\Big(\\
&\qquad\qquad \Big(r\cos(\theta) - \sqrt{(AlongYTubeNr - OffSetFiber)^2 + (xrc - v\,t)^2}\,\Big)^2 \\
&\qquad\qquad + (r\sin(\theta))^2,\,\sigma,\,mn\Big)\,r\,\partial\theta\,\partial r\Big]
\end{aligned}
\tag{20}
$$

XCross and YCross are the x and y coordinates for the crossing point between the FCM fiber loop and one of the current cylinders. θs and θp are the angles between the two crossing points relative to the fiber loop and cylinder. It can be seen from figure 10 that crossing points are symmetric around the x−axes of a new coordinate system that is defined by the line that goes through the centers of the fiber loop and current cylinder. This approach is used in the equations below which lists the crossing coordinates and the corresponding angles. Also listed are the two area functions Ap(...) and Asb1(...). Ap gives the area of a cylinder with a radius Rp, while Asb1 calculates the area of the part of the fiber loop that is in the cylinder, corresponding to case 2 above. See fig. 10.

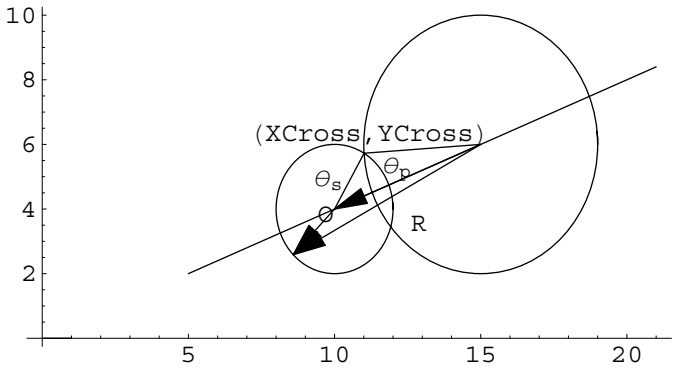

Fig 10. The small circle represents the fiber loop moving along the x – axes. The big circle represnets a current cylinder.

$$\text{XCross}(\text{xrc}, \text{t}, \text{Rp}, \text{AlongYTubeNr}) = \frac{(\text{AlongYTubeNr} - \text{OffSetFiber})^2 + \text{Rp}^2 - \text{rs}^2 + (\text{v t} - \text{xrc})^2}{2\sqrt{(\text{AlongYTubeNr} - \text{OffSetFiber})^2 + (\text{v t} - \text{xrc})^2}}$$

$$\text{YCross}(\text{xrc}, \text{t}, \text{Rp}, \text{AlongYTubeNr}) = -\frac{1}{2}\sqrt{\left(-\left((\text{Rp}^2 - \text{rs}^2)^2 + ((\text{AlongYTubeNr} - \text{OffSetFiber})^2 + (\text{v t} - \text{xrc})^2)^2 - 2(\text{Rp}^2 + \text{rs}^2)((\text{AlongYTubeNr} - \text{OffSetFiber})^2 + (\text{v t} - \text{xrc})^2)\right)\Big/((\text{AlongYTubeNr} - \text{OffSetFiber})^2 + (\text{v t} - \text{xrc})^2)\right)}$$

$$\theta\text{p}(\text{xrc}, \text{t}, \text{Rp}, \text{AlongYTubeNr}) = 2\tan^{-1}\left(\frac{|\text{YCross}(\text{xrc}, \text{t}, \text{Rp}, \text{AlongYTubeNr})|}{|\text{XCross}(\text{xrc}, \text{t}, \text{Rp}, \text{AlongYTubeNr})|}\right)$$

$$\theta\text{s}(\text{xrc}, \text{t}, \text{Rp}, \text{AlongYTubeNr}) = 2\tan^{-1}\left(|\text{YCross}(\text{xrc}, \text{t}, \text{Rp}, \text{AlongYTubeNr})|\Big/\left||\text{XCross}(\text{xrc}, \text{t}, \text{Rp}, \text{AlongYTubeNr})| - \sqrt{(\text{AlongYTubeNr} - \text{OffSetFiber})^2 + (\text{xrc} - \text{v t})^2}\right|\right)$$

$$\text{Ap}(\text{Rp}) = \pi\,\text{Rp}^2$$

$$\begin{aligned}\text{Asb1}(\text{xrc}, \text{t}, \text{Rp}, \text{AlongYTubeNr}) = {}& \text{Which}(|\text{v t}| > |\text{xrc} - |\text{XCross}(\text{xrc}, \text{t}, \text{Rp}, \text{AlongYTubeNr})|| \wedge \\ & |\text{v t}| < |\text{xrc} + |\text{XCross}(\text{xrc}, \text{t}, \text{Rp}, \text{AlongYTubeNr})||, \\ & 0.5(\theta\text{p}(\text{xrc}, \text{t}, \text{Rp}, \text{AlongYTubeNr}) - \\ & \quad \sin(\theta\text{p}(\text{xrc}, \text{t}, \text{Rp}, \text{AlongYTubeNr})))\,\text{Rp}^2 + \\ & \pi\,\text{rs}^2 - 0.5\,\text{rs}^2(\theta\text{s}(\text{xrc}, \text{t}, \text{Rp}, \text{AlongYTubeNr}) - \\ & \quad \sin(\theta\text{s}(\text{xrc}, \text{t}, \text{Rp}, \text{AlongYTubeNr}))), \\ & |\text{v t}| \le |\text{xrc} - |\text{XCross}(\text{xrc}, \text{t}, \text{Rp}, \text{AlongYTubeNr})|| \vee \\ & |\text{v t}| \ge |\text{xrc} + |\text{XCross}(\text{xrc}, \text{t}, \text{Rp}, \text{AlongYTubeNr})||, \\ & 0.5(\theta\text{p}(\text{xrc}, \text{t}, \text{Rp}, \text{AlongYTubeNr}) - \\ & \quad \sin(\theta\text{p}(\text{xrc}, \text{t}, \text{Rp}, \text{AlongYTubeNr})))\,\text{Rp}^2 + \\ & 0.5\,\text{rs}^2(\theta\text{s}(\text{xrc}, \text{t}, \text{Rp}, \text{AlongYTubeNr}) - \\ & \quad \sin(\theta\text{s}(\text{xrc}, \text{t}, \text{Rp}, \text{AlongYTubeNr})))) \quad (21)\end{aligned}$$

Some new parameters have been introduced in the equations above. The meaning of these parameters are

xrc: the position of the cylinder along the x−axes
OffSetFiber: the distance between the global x−axes and the satellite trajectory
AlongYTubeNr: number of the cylinder along the y−axes
Rp: radius of the cylinder
rs: radius of the fiber loop

The equations listed above gives a insight into how the FCM current response are calculated. All of the details of the simulation can be found in appendix B.

4.5 FCM and magnetometer simulation results

Figure 11 to 14 show the results of the simulation. The satellite has here moved along the x axis (offset=0), through the 4 center cylinders of the 20 current cylinders shown in figure 5. The red line in figure 11 is the model current density along the satellite path and the blue line is the current density as measured by the FCM. The interesting quantity is the difference between the model and the measurement. Figure 12 shows the difference betweeen the model and the current density "measured" by the FCM.

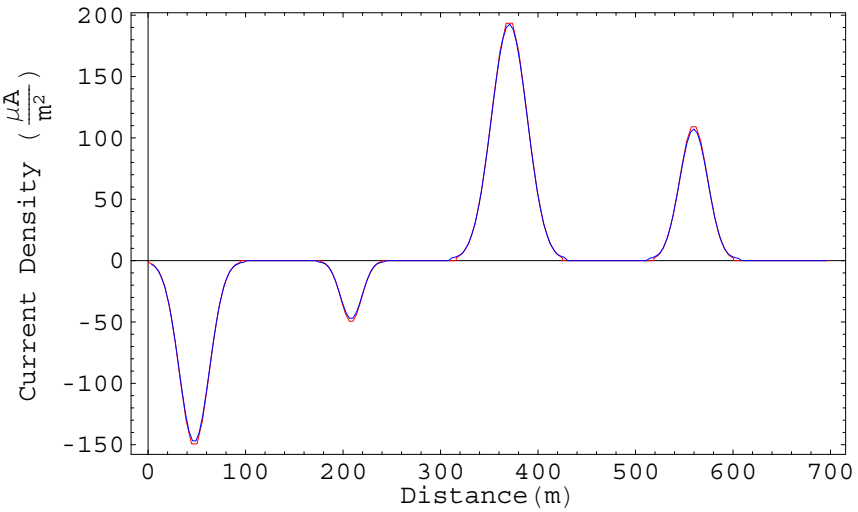

Fig 11. The model and the measured current density for a fiber loop moving along the x−axes.

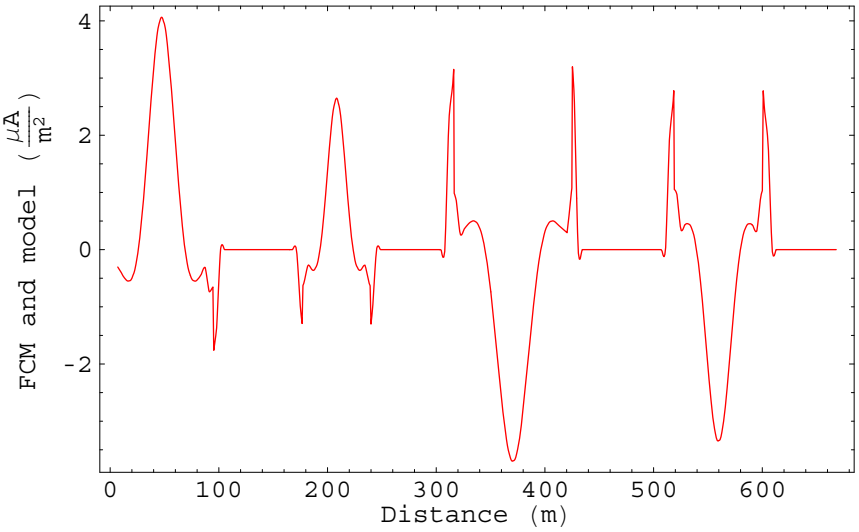

Fig 12. The error of the measured current density as a function of distance along the x−axes.

It is seen from the figures that, in this case, the errors are 4 $\frac{\mu A}{m^2}$ or less. The error peaks that occur at the edges of the tubes are due to the discontinuities in the model current density at the tube−edges.The current density at the edges is set to fall off to 2−10% of the maximum current density in the pipe. When the center of the fiber loops are just outside a pipe almost half of the loop is still inside the pipe and there will be a current through it. Therefore the sharp peaks are due to the simulation model and they are not expected in a real satellite borne FCM unless the real current structures in the magnetosphere/ionosphere also change abroubtly at scales less than 10 meter (the scala size of the FCM fiber loop).

Since the satellite moves on a straight line (locally), the x−axesin our coordinate system, it is only possible to estimate the derivative of the magnetic field with respect to this direction, the x direction. Therefore the expression for the current density reduces to

$$J_z = \nabla \times \overline{H} = \frac{\partial H_y}{\partial x} \quad (22)$$

The next two figures display the y component of the magnetic field along the satellite track when the offset is zero, and the corresponding current density measured by the satellite magnetometer.

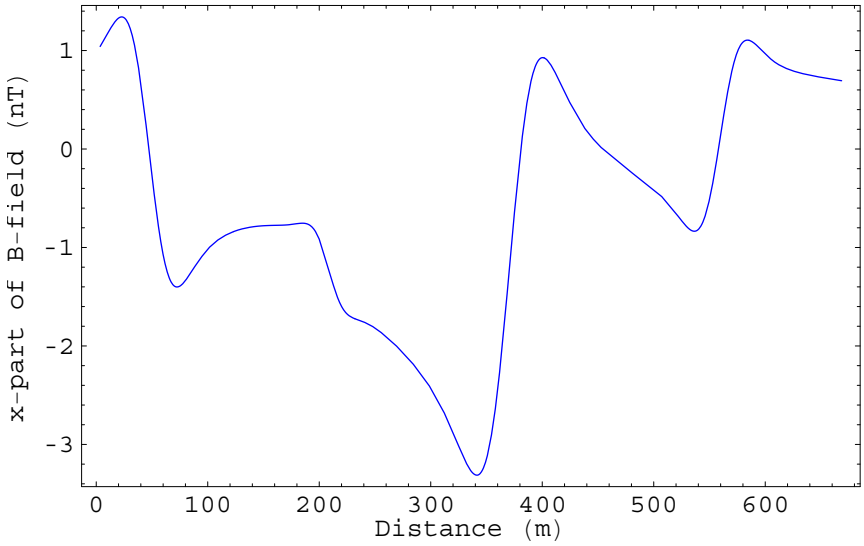

Fig 13. The y−component(not x as the figure says) of the B−fieldmeasured by the magnetometer.

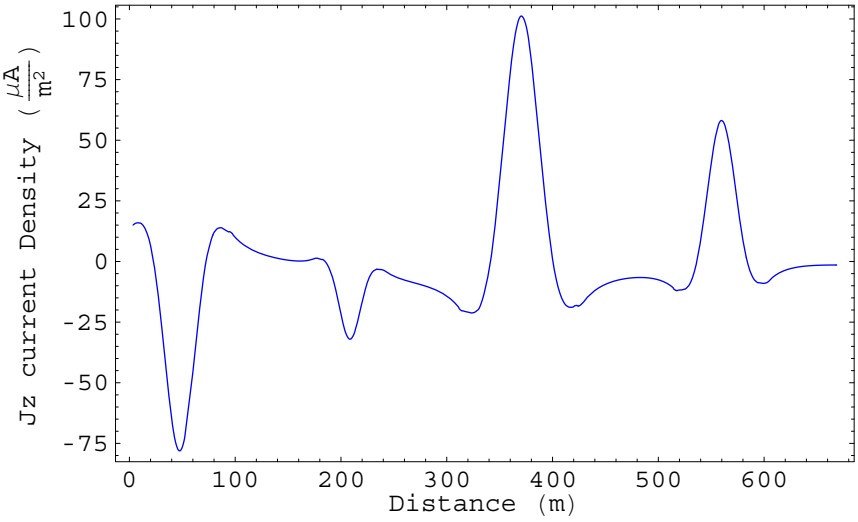

Fig 14. The current density measured by the magnetometer.

In the next figure the red boxes indicate the position of the tubes, the red curve is the model current distribution, the black curve is the FCM simulation result and finally the blue curve shows the magnetometer result.

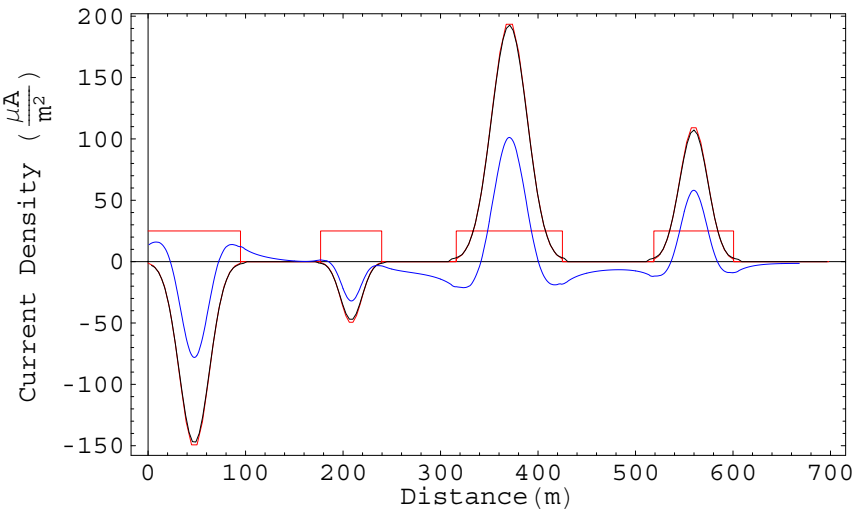

Fig 15. Comparison of the simulated current densities from the FCM and magnetometer.

It is clearly seen from the simulations that the FCM instrument is much more precise compared to the magnetometer, both in determining the absolute values and the shape of the current distribution.

The influence of the tube sizes and the distances between the tubes on the FCM and magnetometer error levels can be seen from figure 16. This figure shows 4 pairs of plots for the following 4 scale sizes:

1. pair. Diameters of and distances between cylinders are random values within the interval 25−50 meter.
2. pair. Diameters of and distances between cylinders are random values within the interval 50−100 meter.
3. pair. Diameters of and distances between cylinders are random values within the interval 100−500 meter.
4. pair. Diameters of and distances between cylinders are random values within the interval 500−2000 meter.

Each pair displays the difference between the FCM simulation and the model current density and the difference between the magnetometer simulation and the model current density. It should be noted that the 4 pairs is taken from 4 different model setups, it is not exactly the same tubes that have been scaled. It is seen, as expected, that the FCM error is very dependent on the values of the tube diameters and distances. The magnetometer errors are larger than the FCM errors and not very dependent on the values of the tube diameters and distances. The magnetometer error is due to the fact that the x−part of the magnetic field can not be neglected. This is not the case for the rectangular current structures below, and we therefore expect to see must lower magnetometer errors for the rectangular current structures.

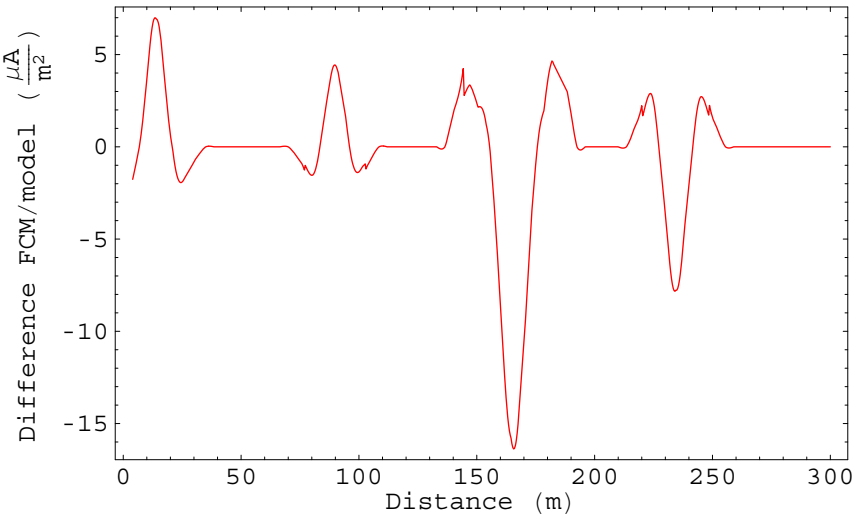
Difference FCM/model (μA / m²)
5
0
-5
-10
-15
0
50
100
150
200
250
300
Distance (m)

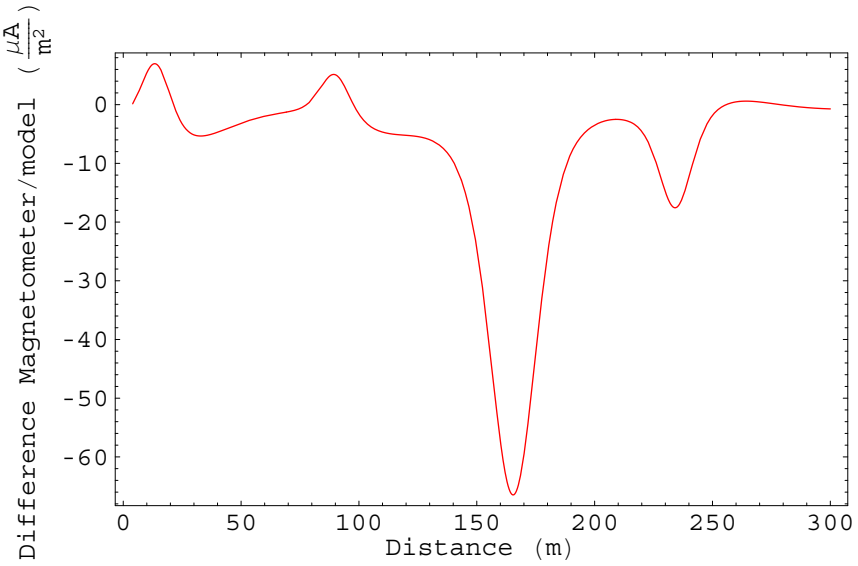
Difference Magnetometer/model (μA / m²)
0
-10
-20
-30
-40
-50
-60
0
50
100
150
200
250
300
Distance (m)

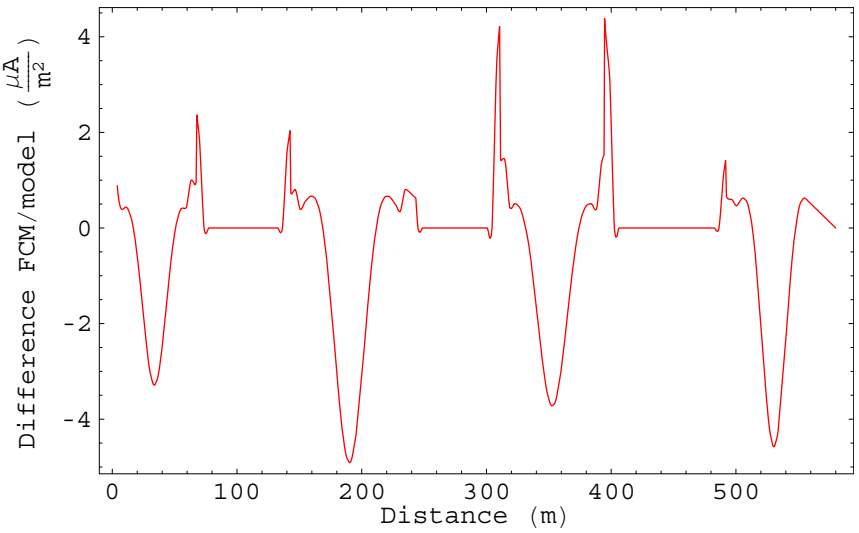
Difference FCM/model (μA / m²)
4
2
0
-2
-4
0
100
200
300
400
500
Distance (m)

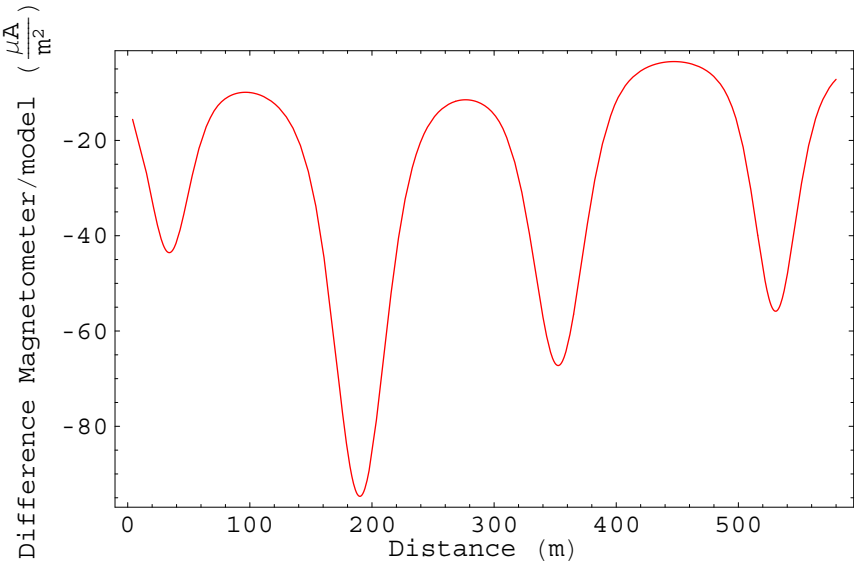
Difference Magnetometer/model (μA / m²)
-20
-40
-60
-80
0
100
200
300
400
500
Distance (m)

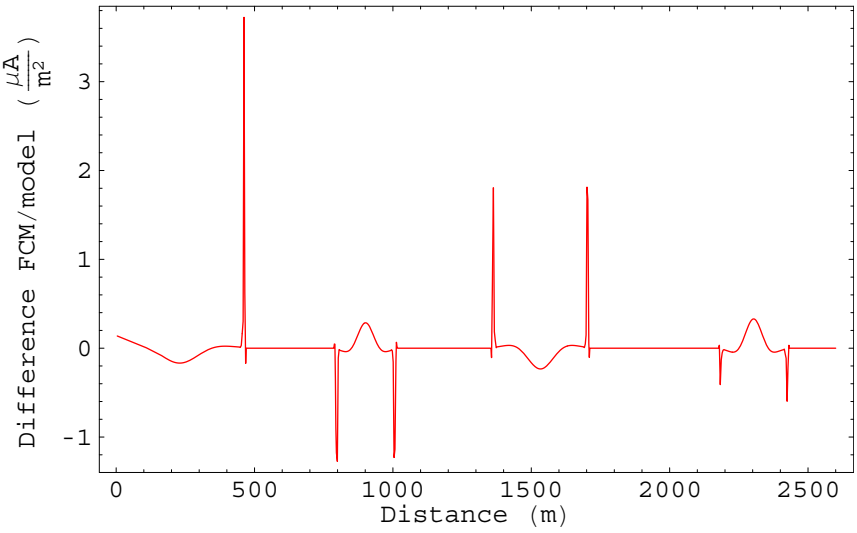
Difference FCM/model (μA / m²)
3
2
1
0
-1
0
500
1000
1500
2000
2500
Distance (m)

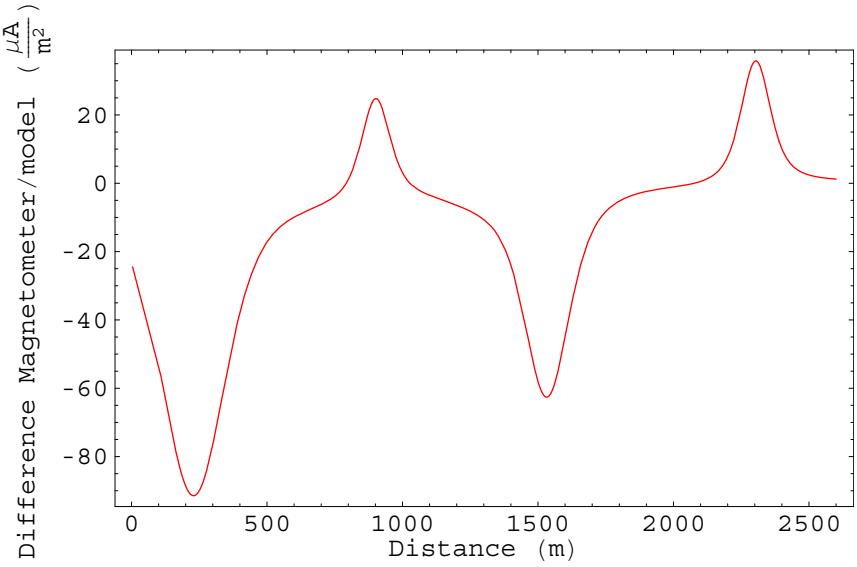
Difference Magnetometer/model (μA / m²)
20
0
-20
-40
-60
-80
0
500
1000
1500
2000
2500
Distance (m)

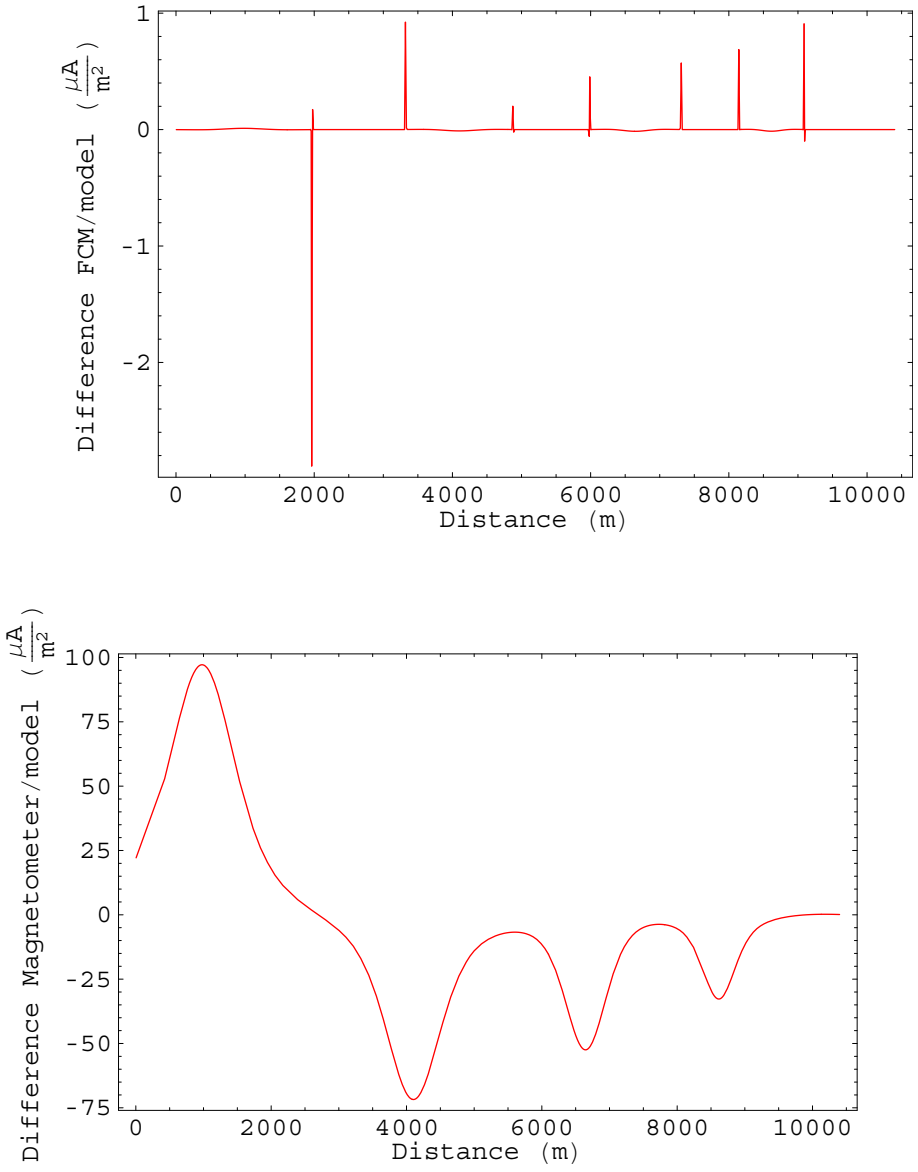

Fig 16. FCM and magnetometer errors for 4 different scale sizes of current structures.

4.6 Current Sheets

It is often assumed that ionospheric current structures are greater in the east−west direction than the north−south direction. The structures are then better characterized as "sheets". The current filaments at low altitudes (1000 km) change structure and become current sheets at higher altitudes (8000 km). The current cylinder model has therefore been extended to perform simulations using current sheets. A Gaussian current distribution only depending on the distances in the x−direction is assumed in the current sheet model. The sheets are assumed to extend to infinity in the y and z directions. Figure 17 shows a model of four current sheets. The 2D (x−y plane) and 3D magnetic field, that corresponds to this current density model, are shown in figure 18 and 19.

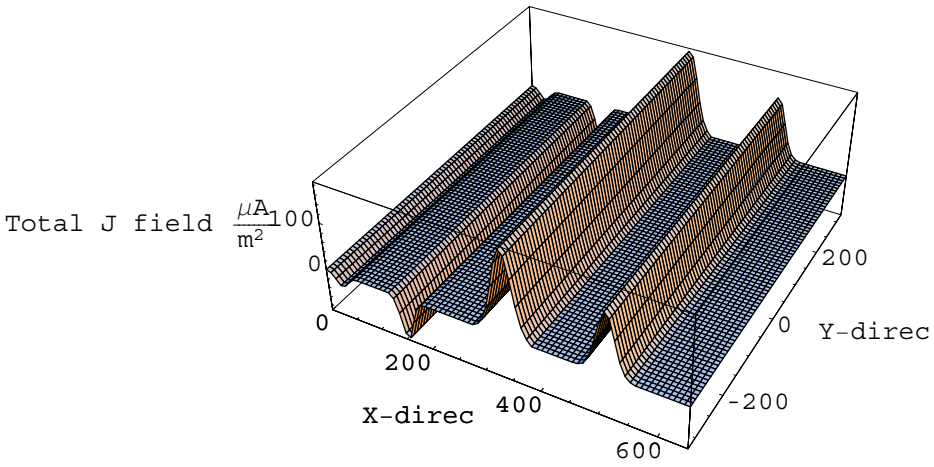

Fig 17. Model current distribution in the case of current sheets.

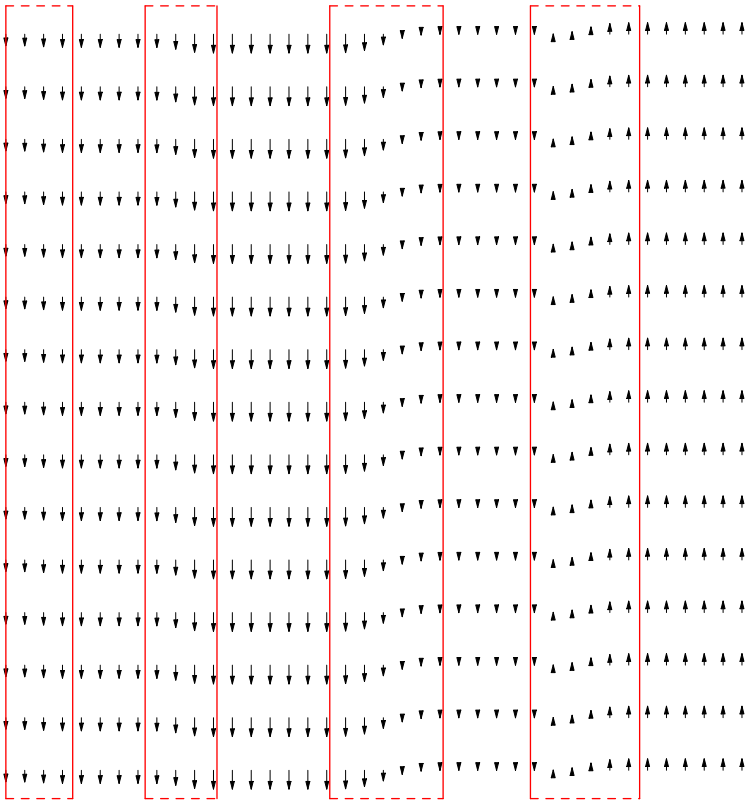

Fig 18. The 2D magnetic field corresponding to the current sheets in fig. 17. The solid and dotted red lines indicate the current sheet structures.

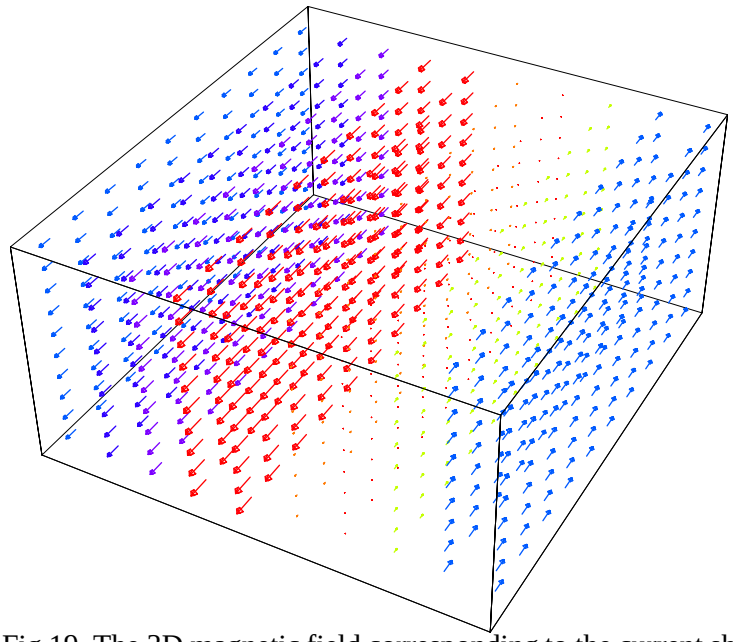

Fig 19. The 3D magnetic field corresponding to the current sheets in fig. 17.

The assumption of Gaussian current density makes it possible to get an explicit expression for the total magnetic field. The magnetic field from one of the current sheets can be found from Amperes law on differential form, when it is assumed that the field is parallel to the current structures (must be so due to symmetry). The field from one current sheet can be expressed as

$$\text{ModelH}(x, \sigma, mn, rc) = mn \sqrt{\frac{\pi}{2}}\, \sigma\, \text{erf}\left(\frac{x}{\sqrt{2}\,\sigma}\right) \quad (23)$$

where erf is the error function. The expression for the total magnetic field from all of the current sheets (the TubeCount number gives us the number of sheets) is

$$\text{VecModelH}(x, y) = \sum_{i=1}^{\text{TubeCount}} \text{ModelH}(x - \text{BigN}[i, 2], \sigma[i], mn[i], r[i])\{0, 1\} \quad (24)$$

This equation has been used to generate the plots in figure18 and 19.

The FCM response is calculated as before and once again yield a rather precise current measurement as seen in figure 20 and 21. The simulation setup parameters are given in section 4.0. The FCM equations in the case of current sheets are the same as the equations in section 4.4 when the factor of 2 is removed. This can be seen from figure 10, when the circular current filament is replaced with a rectangular current sheet.

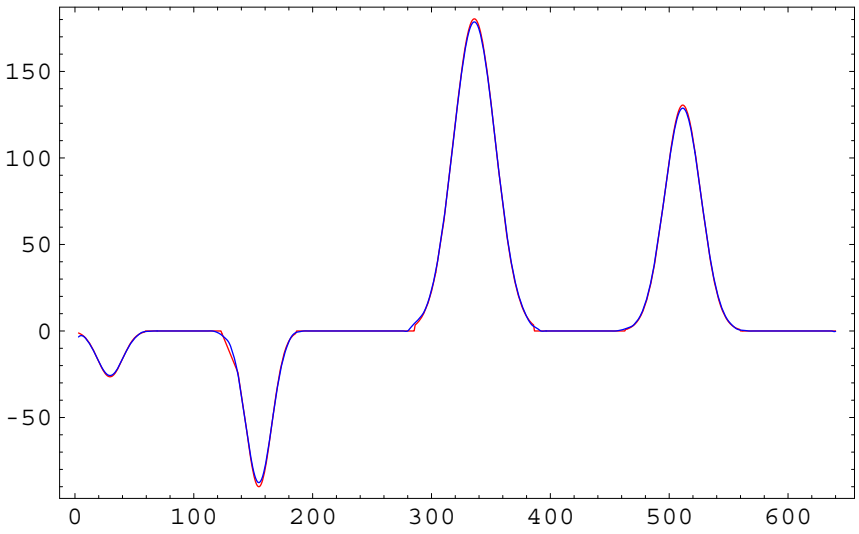

Fig 20. The FCM current density response and the model current density are shown here.

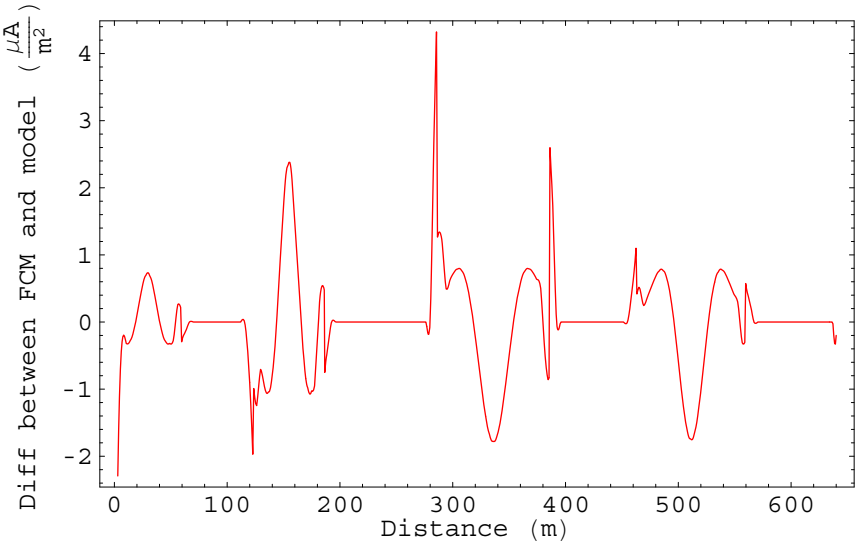

Fig 21. The plot shows the difference between the FCM response and the model current density.

The total magnetic H−field and the magnetometer response are calculated and the results are shown in figure 22 and 23.

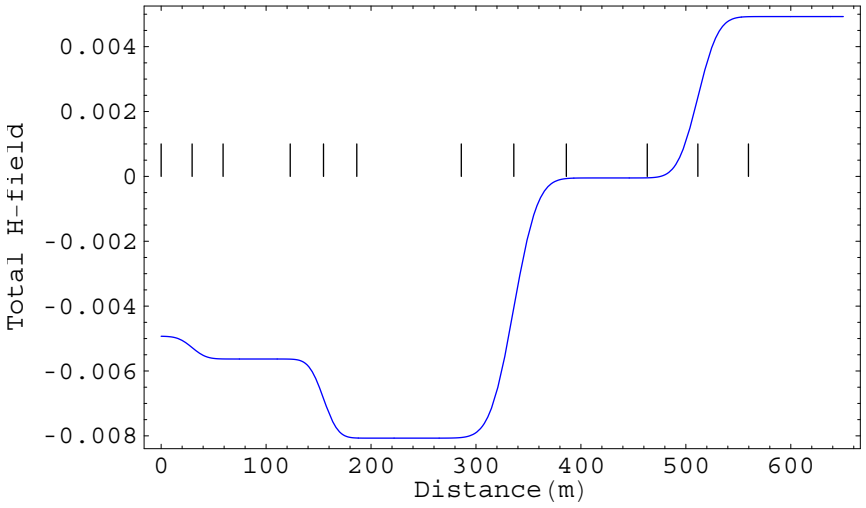

Fig 22. The total magnetic H−field (for the 4 current sheets) as a function of distance. The 4 pairs of 3 lines indicate the positions of the center and the two edges of the current sheet.

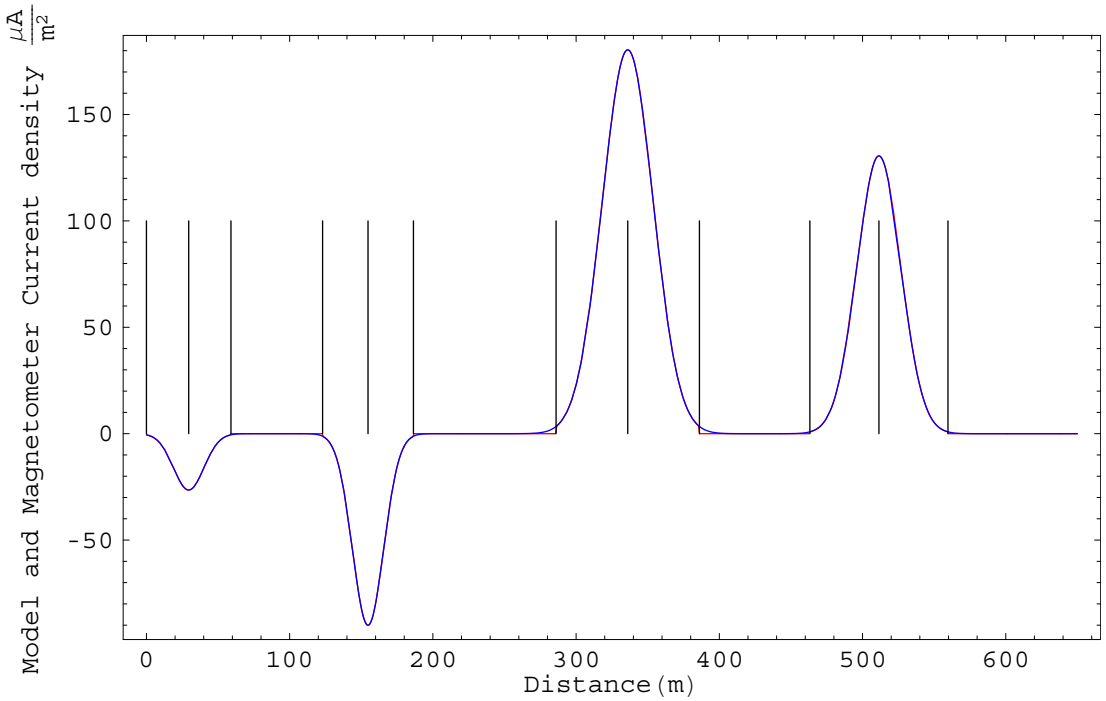

Fig 23. The magnetometer current density response and the model are shown here. The 4 pairs of 3 lines indicate the positions of the center and the two edges of the current sheet.

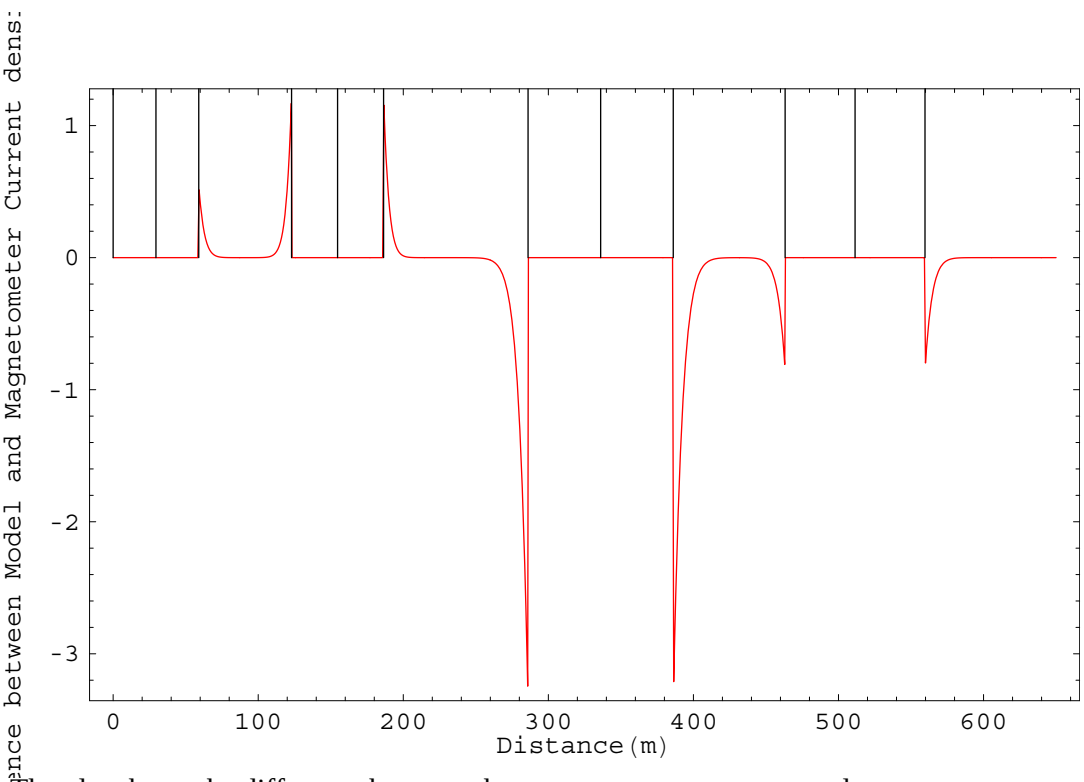

Fig 24. The plot shows the difference between the magnetometer response and the model current density.

Figure 24 shows the corresponding difference between the magnetometer response and the model current density. The magnetometer error is zero except just outside the tubes. These errors are caused by numeric errors when the magnetic field is differentiated to give the current response of the magnetometer.

For this highly idealized setup a manetometer should yield exact measurements. The reason for this is, that the magnetic field only has one component and this component is assumed perpendicular to the velocity of the satellite. This can only be realized if the current structures extend to infinity in the direction of the y and z axes.

5.0 Conclusion

We have in this report compared the FCM and magnetometer responses. This comparison has been done with the use of computer simulations. It has been showed that the FCM instrument is superior to the magnetometer instrument in determining the current density in ionospheric/magnetospheric current structures. The performance of the two instruments are however comparable in the case of very large current sheets (when they are hit head on).

References

Akasofu, S.−I.,Dynamics of the Magnetosphere, Reidel Publishing Company, 1980.

Akasofu, S.−I.,"The Dynamic Aurora", Scientific American, p 90−97,may 1989.

Akasofu, S.−I.,Y. Kamide, J.R. Kan, L.C. Lee, B.−H.Ahn, Power Transmission from the Solar Wind−MagnetosphereDynamo to the Magnetosphere and to the Ionosphere: Analysis of the IMS Alaska Meridian Chain Data, Planet. Space Sci., 29, 721, 1981.

Arnoldy, R.L., Auroral Particle Precipitation and Birkeland Currents, Rev. Geophys. Space Phys., 12, 217, 1974.

Bankov, L., N. Bankov, A. Bochev, I. Kutiev, L. Todorieva, E.M. Dubinin, I.M. Podgorny, and Yu.N. Potanin, Suprathermal Electrons in Small−ScaleField−Aligned Currents, Geophys. Res. Lett., 13, 105−108,1986.

Blomberg, L.G., G.T. Marklund, P.−A.Lindqvist, and L. Bylander, EMMA −The Electric and Magnetic Field Instrument on ASTRID−2,Royal Institute of Technology Report, ALP−97−04,1997.

Burke W.J., M. Silevitch, and D.A. Hardy, Observations of Small−Scale Auroral Vortices by the S3−2Satellite, J. Geophys. Res., 88, 3127−3137,1983.

Burke, W.J., Electric Fields, Birkeland Currents and Electron Precipitation in the Vicinity of Discrete Auroral Arcs, in Physics of Auroral Arc Formation, S.−I.Akasofu and J.R. Kan (Eds.), Geophys. Monograph, 1981.

Elbek, B., "Elektromagnetisme", Niels Bohr Insitutet, Denmark, 1994.

Fung, S.F. and R. A. Hoffman, "Finite geometry effects of field−alignedcurrents", JGR vol.97 p.8569−8579,1992.

Fälthammar, C.−G.,"Space Physics", Alfvén Laboratory, Royal Institute of Technology, Sweden, 1995.

Hardy, D.A., Auroral Dynamics During a Substorm Near the Dawn−DuskMeridian, EOS, 60, 358, 1979.

Heikkila, W.J., Outline of a Magnetosphere Theory, J. Geophys. Res., 79, 2496, 1974.

Holmegaard, H., "A Statistical Study of Ionospheric Field Aligned Currents Estimated from Magnetic Satellite Measurements", M.Sc.Thesis, Dep. of Geoph., NBIfAFG, University of Copenhagen, 1998.

Høeg,P., A. Hauchecorne, G. Kirchengast, S. Syndergaard, B. Belloul, R. Leitinger, W. Rothleitner, Derivation of Atmospheric Properties Using a Radio Occultation Technique, Danish Meteorological Institute, Scientific Report, No. 95−4, Copenhagen, Denmark, 1995.

P. Høeg,G. Bergeton Larsen, H.−H.Benzon, J. Grove−Rasmussen,S. Syndergaard, M. Dahl Mortensen, J. Christensen, and K. Schultz, GPS Atmosphere Profiling Methods and Error Assessments. Danish Meteorological Institute, Scientific Report, No. 98−7,Copenhagen, Denmark, 1998.

Iijima, T., and T.A. Potemra, Large−Scale Characteristics of Field−Aligned Currents Associated with Substorms, J. Geophys. Res., 83, 599−615,1978.

Iijima, T. and T. A. Potemra, "The amplitude distribution of field−aligned currents at northern high latitudes observed by TRIAD", JGR, 81, 2165−2174,1976.

Kamide, Y. et al., Global Distribution of Ionospheric and Field−AlignedCurrents During Substorms as Determined from Six IMS Meridian Chains of Magnetometers: Initial Results, J. Geophys. Res., 87, 8228−8240,1982.

Kamide, Y., The Relationship Between Field−Aligned Currents and the Auroral Electrojets, Space Sci. Rev., 31, 127−243,1982.

Kivelson, M. G. and C. T. Russell, "Introduction to space physics", Cambridge University Press 1995.

Lühr, H., J. F. Warnecke and M. K. A. Rother, "An Algorithm for Estimating Field Aligned Currents from Single Spacecraft Magnetic Field Measurements: A Diagnogstic Tool Applied to Freja Satellite Data", IEEE transactions on geoscience and remote sensing, vol 34 no 6, 1996.

Lühr, H., J. Warnecke, L.J. Zanetti, P.A. Lindquist, and T.J. Hughes, Fine Structure of Field−Aligned Current Sheets Deduced from Spacecraft and Ground−based Observations: Initial FREJA Results. Geophys. Res. Lett., 21, 1883, 1994.

Lyons, L.R., Generation of Large−scaleRegions of Auroral Currents, Electric Potentials and Precipitation by the Divergence of the Convection Electric Field, J. Geophys. Res., 85, 17, 1980.

Marklund, G.T., L.G. Blomberg, P.−A.Lindqvist, C.−G.Fälthammar, G. Haerendal, F.S. Mozer, A. Pedersen, and P. Tanskanen, The Double Probe Electric Field Experiment on FREJA: Experiment Description and First Results, Space Sci. Rev., 70, 483−508,1994.

Marklund, G.T., L.G. Blomberg, L. Bylander, and P.−A.Lindqvist, ASTRID−2:A Low−Budget Microsatellite Mission for Auroral Research, ESA, SP−397,1997.

Moretto, T. and N. Olsen, "Jordens Magnetfelt set fra rummet" Kvant, Denmark, 1998.

Olsen, L., "Beliggenhed og styrke af feltrettede strømsystemer i nordlyszonen bestemt med magnetiske satellitdata", Geofysisk afdeling, NBIfAFG, Københavns Universitet, 1999.

Potemra, T.A., Current Systems in the Earth's Magnetosphere, Rev. Geophys. and Space Phys., 17, 640, 1979.

Potemra, T.A., (Ed.), Magnetospheric Currents, Geophys. Monograph, 28, 1984.

Potemra, T.A., L.J. Zanetti, P.F. Bythrow, and A.T.Y. Lui, By−DependentConvection Patterns During Northward Interplanetary Magnetic Field, J. Geophys. Res., 89, 9753−9760,1984.

Primdahl, F., A. Bahnsen, M. Ejiri, P. Høeg,G. Marklund, B.N. Mæhlum, J.K. Olesen, E. Ungstrup, and L.J. Zanetti, Rocket−borne and Ground−based observations of Coincident Field−alignedCurrents, Electron Beams, and Plasma Density Enhancements in the Afternoon Auroral Oval, Planet. Space Sci., 32, 561−583,1984.

Primdahl, F., P. Høeg,C.J. Nielsen and J.E. Schrøder,A New Method for Measuring Space Plasma Current Densities by the Faraday Rotation of Laser Light in Optical Monomode Fibers, DRI Scientific Report, 4−86,1986.

Primdahl, F., P. Høeg,C. J. Nielsen and J. E. Schrøder,"A New Method for Measuring Space Plasma Current Densities by the Faraday Rotation of Laser Light in Optical Monomode Fibers", Danish Space Research Institute, 1986.

Spiro et al., Quantitative Simulation of a Magnetospheric Substorm, 3, Plasmaspheric Electric Fields an Evolution of a Plasmapause, J. Geophys. Res., 86, 2261, 1981.

Stasiewicz, K., and T. Potemra, Multiscale Current Structures Observed by Freja, J. Geophys. Res., 103, 4315−4325,1998.

Stasiewicz, K., G. Holmgren and L. Zanetti, Density Depletions and Current Singularities Observed by Freja, J. Geophys. Res., 103, 4251−4260,1998.

Stasiewicz, K., and T. Potemra, "Multiscale current structures observed by Freja", JGR vol 103 p 4315−4325,1998.

Stern, D.P., The Origins of Birkeland Currents, Rev. Geophys. & Space Phys., 21, 125, 1983.

Sugiura, M., N.C. Maynard, W.H. Farthing, J.P. Heppner, B.G. Ledley, and J.L. Cahill, Initial Results on the correlation between the Magnetic and Electric Fields

Observed from the DE−2 Satellite in the Field−aligned Current Regions, Geophys. Res. Lett., 9, 985−988,1982.

Sugiura M., et al , "Initial results on the correlation between the magnetic and electric fields observed form the DE−2 satellite in the field aligned current regions", Geophys. Res. Let., vol 9, p 985, 1982.

Vasyliunas, V.M., The Interrelationship of Magnetospheric Processes, in Earth's Magnetospheric Processes, B.M. McCormac (Ed.), Reidel Publishing Company, 1972.

Zanetti, L.J. et al., Ionospheric and Birkeland Current Distributions Inferred from the MAGSAT Magnetometer Data, J. Geophys. Res., 88, 4875, 1983.

Appendix A

This appendix gives the *Mathematica* code for the model setup.

```
    my0 = 1.25664 × 10^-6;
  N1 = 2;
  N2 = 2;
  Nxp = 2;
  Nxn = 2;
  TotalPipes = (Nxp + 1 + Nxn) (N1 + N2);
  r = Array[a, {TotalPipes}];
  L = Array[b, {TotalPipes}];
  JMean = Array[cm, {TotalPipes}];
  JSDev = Array[cs, {TotalPipes}];
  BinJ = Array[d, {TotalPipes}];
  PDiaMax = 55 2;
  PDiaMin = 25 2;
  DisMax = 50 2;
  DisMin = 25 2;
  CurDenMaxMeanV = 200;
  CurDenMinMeanV = 10;
  CurDenMaxSDev = 150 1.5;
  CurDenMinSDev = 50 2;
  (* CurDenMinSDev=0.5; *)
  rlimMin = 0.01 / 2;
  rlimMax = 0.05 / 2;
  q = Table[Random[Real, {rlimMin, rlimMax}], {TotalPipes}];
  TmpRan1 = Array[ert, {TotalPipes}];
  For[i = 1, i <= TotalPipes, i++, TmpRan1[[i]] = Random[];];
  For[i = 1, i <= TotalPipes, i++,
   r[[i]] = ((PDiaMax - PDiaMin) * TmpRan1[[i]] + PDiaMin) / 2;]
  For[i = 1, i <= TotalPipes, i++, L[[i]] = (DisMax - DisMin) * Random[] + DisMin;]
  For[i = 1, i <= TotalPipes, i++, JMean[[i]] =
      ((CurDenMaxMeanV - CurDenMinMeanV) * TmpRan1[[i]] + CurDenMinMeanV) 10^-6;]
  For[i = 1, i <= TotalPipes, i++, JSDev[[i]] = Sqrt[ -r[[i]]^2 / (2 Log[ q[[i]] JMean[[i]] / JMean[[i]] ]) ];]
  LimRand1 = 0.8;
  LimRand2 = 1 - LimRand1;
  z = 0;
  For[j = 1, j <= Nxp + 1 + Nxn, j++,
For[i = 1, i <= N1, i++, tmp = Random[];
    z = z + 1; If[tmp >= LimRand1, BinJ[[z]] = 1, BinJ[[z]] = -1]];
For[i = N1 + 1, i <= N1 + N2, i++, tmp = Random[]; z = z + 1;
    If[tmp >= LimRand2, BinJ[[z]] = 1, BinJ[[z]] = -1]];]
  J1tmp = 0.0;
  J2tmp = 0.0;
  For[i = 1, i <= N1, i++, J1tmp = JMean[[i]] * BinJ[[i]] + J1tmp;]
  For[i = N1 + 1, i <= N1 + N2, i++, J2tmp = JMean[[i]] * BinJ[[i]] + J2tmp;]
  Print[AveJ1: , (J1tmp / N1) 10^6];
  Print[AveJ2: , (J2tmp / N2) 10^6];
  AlongY = Array[Aly, {(Nxp + 1 + Nxn) (N1 + N2)}];
  For[i = 1, i <= N1 + N2, i++, AlongY[[i]] = 0;];
  z = N1 + N2;
```

```
    For[j = 1, j <= Nxn, j++, tmprand1 = Random[]; tmprand2 = Random[];
      tmpdis = AlongY[[z]]; For[i = 1, i <= N1 + N2, i++, z = z + 1;
       AlongY[[z]] = -(((PDiaMax - PDiaMin) * tmprand1 + PDiaMin) / 2 +
              (DisMax - DisMin) * tmprand2 + DisMin) + tmpdis;]];


    For[j = 1, j <= Nxp, j++, tmprand1 = Random[]; tmprand2 = Random[];
      If[j == 1, tmpdis = 0;, tmpdis = AlongY[[z]];]; For[i = 1, i <= N1 + N2, i++,
       z = z + 1; AlongY[[z]] = ((PDiaMax - PDiaMin) * tmprand1 + PDiaMin) / 2 +
          (DisMax - DisMin) * tmprand2 + DisMin + tmpdis]];
    AlongY
    BigN = Array[A, {(Nxp + 1 + Nxn) (N1 + N2), 8}];
    z = 0;
    For[j = 1, j <= 1 + Nxn + Nxp, j++,
tmpdis = 0.0;
For[i = 1, i <= N1 + N2, i++, z = z + 1; BigN[[z, 1]] = tmpdis;
      BigN[[z, 2]] = r[[z]] + BigN[[z, 1]]; BigN[[z, 3]] = r[[z]] + BigN[[z, 2]];
      BigN[[z, 4]] = L[[z]] + BigN[[z, 3]]; tmpdis = BigN[[z, 4]];
      BigN[[z, 5]] = JMean[[z]] * BinJ[[z]]; BigN[[z, 6]] = JSDev[[z]];
      BigN[[z, 7]] = BigN[[z, 5]] π (BigN[[z, 3]] - BigN[[z, 2]])^2;
      BigN[[z, 8]] = BinJ[[z]];]]


    rs = 5;
fs = 4000 / 2;
v = 7000;
S = BigN[[N1 + N2, 4]]
NN = IntegerPart[S fs / v]
ResultMatrix = Array[e, {NN, 2}];
RHphiMtx = Array[he, {NN, 2}];
Δt = 1 / fs // N
T = S / v // N
xxxResultMatrix = Array[xxxe, {NN, 2}];
xxxRHphiMtx = Array[xxxhe, {NN, 2}];
rs = 5;
```

Appendix B

This appendix gives the *Mathematica* code for the implementation of the FCM simulation calculations.

```
    Gaus[x_, μ_, σ_, mn_] := mn Exp[-(x - μ)^2 / (2 σ^2)]
NewGaus[x_, σ_, mn_] := mn Exp[-(x) / (2 σ^2)]
OffSetFiber = 0;
TubeCount = TotalPipes
FindXinBigN[x_, j_] := Which[((AlongY[[j]] + r[[j]] > OffSetFiber) &&
       (AlongY[[j]] - r[[j]] < OffSetFiber) && (x >= BigN[[j, 1]]) &&
      (x <= BigN[[j, 3]]) && (x - rs >= BigN[[j, 1]]) && (x + rs <= BigN[[j, 3]])),
   Case = 2, ((AlongY[[j]] + r[[j]] > OffSetFiber) &&
      (AlongY[[j]] - r[[j]] < OffSetFiber) && (x >= BigN[[j, 3]]) &&
      (x <= BigN[[j, 4]]) && (x - rs >= BigN[[j, 3]]) && (x + rs <= BigN[[j, 4]]) ),
   Case = 4, ((AlongY[[j]] + r[[j]] > OffSetFiber) &&
      (AlongY[[j]] - r[[j]] < OffSetFiber) &&
      (x - rs <= BigN[[j, 1]]) && (x + rs >= BigN[[j, 1]])),
   Case = 3, ((AlongY[[j]] + r[[j]] > OffSetFiber) &&
      (AlongY[[j]] - r[[j]] < OffSetFiber) && (x - rs <= BigN[[j, 3]]) &&
      (x + rs >= BigN[[j, 3]])), Case = 1, True, 22222222];


FindDistanceinBigN[dis_, j_] := Which[((AlongY[[j]] + r[[j]] > OffSetFiber) &&
      (AlongY[[j]] - r[[j]] < OffSetFiber) && (dis + rs <= r[[j]])),
   Case = 2, ((AlongY[[j]] + r[[j]] > OffSetFiber) &&
      (AlongY[[j]] - r[[j]] < OffSetFiber) && (dis - rs >= r[[j]]) &&
      (x - rs >= BigN[[j, 3]]) && (x + rs <= BigN[[j, 4]])),
   Case = 4, ((AlongY[[j]] + r[[j]] > OffSetFiber) &&
      (AlongY[[j]] - r[[j]] < OffSetFiber) &&
      (dis + rs >= r[[j]]) && (dis - rs <= r[[j]])),
   Case = 3, ((AlongY[[j]] + r[[j]] > OffSetFiber) &&
      (AlongY[[j]] - r[[j]] < OffSetFiber) && (dis + rs >= r[[j]]) &&
      (dis - rs <= r[[j]])), Case = 1, True, 22222222];


XCross[xrc_, t_, Rp_, AlongYTubeNr_] :=
  ((AlongYTubeNr - OffSetFiber)^2 + Rp^2 - rs^2 + (v t - xrc)^2) /
    (2 √((AlongYTubeNr - OffSetFiber)^2 + (v t - xrc)^2));


YCross[xrc_, t_, Rp_, AlongYTubeNr_] :=
  -(1/2) √(-((Rp^2 - rs^2)^2 - 2 (Rp^2 + rs^2) ((AlongYTubeNr - OffSetFiber)^2 + (v t - xrc)^2) +
            ((AlongYTubeNr - OffSetFiber)^2 + (v t - xrc)^2)^2) /
       ((AlongYTubeNr - OffSetFiber)^2 + (v t - xrc)^2));


θp[xrc_, t_, Rp_, AlongYTubeNr_] :=
  2 ArcTan[Abs[YCross[xrc, t, Rp, AlongYTubeNr]] / Abs[XCross[xrc, t, Rp, AlongYTubeNr]]];
```

```
θs[xrc_, t_, Rp_, AlongYTubeNr_] :=
  2 ArcTan[Abs[YCross[xrc, t, Rp, AlongYTubeNr]] / Abs[Abs[XCross[xrc, t, Rp,
            AlongYTubeNr]] - Sqrt[(xrc - v t)^2 + (AlongYTubeNr - OffSetFiber)^2]]];

Ap[Rp_] := π Rp^2;

Asb1[xrc_, t_, Rp_, AlongYTubeNr_] :=
  Which[(Abs[v t] > Abs[xrc - Abs[XCross[xrc, t, Rp, AlongYTubeNr]]] &&
      Abs[v t] < Abs[xrc + Abs[XCross[xrc, t, Rp, AlongYTubeNr]]]), 0.5 Rp^2
     (θp[xrc, t, Rp, AlongYTubeNr] - Sin[θp[xrc, t, Rp, AlongYTubeNr]]) + π rs^2 -
    0.5 rs^2 (θs[xrc, t, Rp, AlongYTubeNr] - Sin[θs[xrc, t, Rp, AlongYTubeNr]]),
   (Abs[v t] <= Abs[xrc - Abs[XCross[xrc, t, Rp, AlongYTubeNr]]] ||
      Abs[v t] >= Abs[xrc + Abs[XCross[xrc, t, Rp, AlongYTubeNr]]]),
   0.5 Rp^2 (θp[xrc, t, Rp, AlongYTubeNr] - Sin[θp[xrc, t, Rp, AlongYTubeNr]]) +
    0.5 rs^2 (θs[xrc, t, Rp, AlongYTubeNr] - Sin[θs[xrc, t, Rp, AlongYTubeNr]])];

UStep[argu1_, argu2_] := Which[Abs[argu1] < argu2, -1, Abs[argu1] >= argu2, -1];

NewJCase2[t_, μ_, σ_, mn_, AlongYTubeNr_, xrc_] := NIntegrate[(NewGaus[(r Sin[θ])^2 +
        (r Cos[θ] + UStep[v t, xrc] Sqrt[(xrc - v t)^2 + (AlongYTubeNr - OffSetFiber)^2])^2,
      σ, mn] r), {θ, 0, 2 π}, {r, 0, rs}];

NewJCase13[t_, μ_, σ_, mn_, xrc_, Rp_, AlongYTubeNr_] :=
  2 NIntegrate[(NewGaus[(r)^2, σ, mn] r), {θ, 0, θp[xrc, t, Rp, AlongYTubeNr] / 2},
     {r, 1/Cos[θ] (Abs[XCross[xrc, t, Rp, AlongYTubeNr]]), Rp}]          +
   Which[(Abs[v t] > Abs[xrc - Abs[XCross[xrc, t, Rp, AlongYTubeNr]]] &&
      Abs[v t] < Abs[xrc + Abs[XCross[xrc, t, Rp, AlongYTubeNr]]]),
    Print[v t,   , π - θs[xrc, t, Rp, AlongYTubeNr] / 2,   ,
     2 NIntegrate[(NewGaus[(r Sin[θ])^2 + (r Cos[θ] + UStep[v t, xrc]
          Sqrt[(xrc - v t)^2 + (AlongYTubeNr - OffSetFiber)^2])^2, σ, mn] r),
       {θ, 0, π - θs[xrc, t, Rp, AlongYTubeNr] / 2}, {r, 0, rs}] +
     2 NIntegrate[(NewGaus[(r Sin[θ])^2 + (r Cos[θ] + UStep[v t, xrc]
          Sqrt[(xrc - v t)^2 + (AlongYTubeNr - OffSetFiber)^2])^2, σ, mn] r),
       {θ, 0, θs[xrc, t, Rp, AlongYTubeNr] / 2}, {r, 0,
        1/Cos[θ] (Abs[Abs[XCross[xrc, t, Rp, AlongYTubeNr]] -
            Sqrt[(xrc - v t)^2 + (AlongYTubeNr - OffSetFiber)^2]])}]];
     2 NIntegrate[(NewGaus[(r Sin[θ])^2 + (r Cos[θ] + UStep[v t, xrc]
          Sqrt[(xrc - v t)^2 + (AlongYTubeNr - OffSetFiber)^2])^2, σ, mn] r),
       {θ, 0, π - θs[xrc, t, Rp, AlongYTubeNr] / 2}, {r, 0, rs}] +
```

```
        2 NIntegrate[ (NewGaus[ (r Sin[θ])^2 + (r Cos[θ] + UStep[v t, xrc]
                                  Sqrt[(xrc - v t)^2 + (AlongYTubeNr - OffSetFiber)^2]) ^2, σ, mn] r),
          {θ, 0, θs[xrc, t, Rp, AlongYTubeNr] / 2}, {r, 0, 1/Cos[θ]
            (Abs[Abs[XCross[xrc, t, Rp, AlongYTubeNr]] -
                Sqrt[(xrc - v t)^2 + (AlongYTubeNr - OffSetFiber)^2] ])}],
       (Abs[v t] <= Abs[xrc - Abs[XCross[xrc, t, Rp, AlongYTubeNr]]] ||
          Abs[v t] >= Abs[xrc + Abs[XCross[xrc, t, Rp, AlongYTubeNr]]]),
       2 NIntegrate[ (NewGaus[ (r Sin[θ])^2 + (r Cos[θ] + UStep[v t, xrc]
                                  Sqrt[(xrc - v t)^2 + (AlongYTubeNr - OffSetFiber)^2]) ^2, σ, mn] r),
          {θ, 0, θs[xrc, t, Rp, AlongYTubeNr] / 2}, {r, 1/Cos[θ]
            (Abs[Abs[XCross[xrc, t, Rp, AlongYTubeNr]] -
                Sqrt[(xrc - v t)^2 + (AlongYTubeNr - OffSetFiber)^2] ]), rs}]];

jsave = 1;

tmp1 = 0; tmp2 = 0; tmp3 = 0; tmp4 = 0;

For[i = 1, i <= NN, i++, t = i Δt; ResultMatrix[[i, 1]] = t;
  x = v t; For[j = jsave, j <= TubeCount, j++,
    tmp = FindDistanceinBigN[Sqrt[(BigN[[j, 2]] - v t)^2 + (AlongY[[j]] - OffSetFiber)^2] , j];
    If[ (tmp != 22222222), Switch[tmp, 1, tmp1++; ResultMatrix[[i, 2]] =
        10^6 (NewJCase13[t, BigN[[j, 2]], JSDev[[j]], JMean[[j]] BinJ[[j]],
            BigN[[j, 2]], BigN[[j, 3]] - BigN[[j, 2]], AlongY[[j]]]) /
          Asb1[BigN[[j, 2]], t, BigN[[j, 3]] - BigN[[j, 2]], AlongY[[j]]];
      CaseInform[[i, 1]] = (v Δt i) / 1000; CaseInform[[i, 2]] = tmp;, 2,
      tmp2++; ResultMatrix[[i, 2]] = 10^6 1/(π r_s^2) (NewJCase2[t, BigN[[j, 2]],
          JSDev[[j]], JMean[[j]] BinJ[[j]], AlongY[[j]], BigN[[j, 2]]]);
      CaseInform[[i, 1]] = (v Δt i) / 1000; CaseInform[[i, 2]] = tmp;,
      3, tmp3++; ResultMatrix[[i, 2]] =
        10^6 (NewJCase13[t, BigN[[j, 2]], JSDev[[j]], JMean[[j]] BinJ[[j]],
            BigN[[j, 2]], BigN[[j, 3]] - BigN[[j, 2]], AlongY[[j]]]) /
          Asb1[BigN[[j, 2]], t, BigN[[j, 3]] - BigN[[j, 2]], AlongY[[j]]];
      CaseInform[[i, 1]] = (v Δt i) / 1000; CaseInform[[i, 2]] = tmp;,
      4, tmp4++; ResultMatrix[[i, 2]] = 0.0;
      CaseInform[[i, 1]] = (v Δt i) / 1000; CaseInform[[i, 2]] = tmp;];
    jsave = j; j = TubeCount + 1;, ResultMatrix[[i, 2]] = 0;]]]

For[i = 1, i <= NN, i++, xxxResultMatrix[[i, 1]] = (v Δt i) / 1000;
  xxxResultMatrix[[i, 2]] = ResultMatrix[[i, 2]];]
```

Appendix C

This appendix gives the *Mathematica* code for the implementation of the method 1and 2 calculations of the magnetic field.

```
Gaus[x_, μ_, σ_, mn_] := mn Exp[-(x - μ)^2 / (2 σ^2)]
NewGaus[x , σ , mn ] := mn Exp[-(x) / (2 σ^2)]
ModelH[x_, μ_, σ_, mn_, rc_] :=
 Which[Abs[x - μ] <= rc, (E^((-x^2 + μ)/(2 σ^2)) (-1 + E^(x^2/(2 σ^2))) mn σ^2)/x, Abs[x - μ] > rc, (E^((-rc^2 + μ)/(2 σ^2)) (-1 + E^(rc^2/(2 σ^2))) mn σ^2)/x]
NewModelH[x_, σ_, mn_, rc_] :=
 Which[Abs[x] <= rc, (+(1 - E^(-x^2/(2 σ^2))) mn σ^2)/x, Abs[x] > rc, (+(1 - E^(-rc^2/(2 σ^2))) mn σ^2)/x]
Globalx = 0;
NewNewHphiVer2XAndYCom[t_, μ_, σ_, mn_, yp_, rc_] :=
 1/(2 π) NIntegrate[{(NewGaus[(r Cos[θ])^2 + (r Sin[θ])^2, σ, mn] r)/Sqrt[(Globalx - r Cos[θ])^2 + (v t - μ - r Sin[θ])^2] (v t - μ - r Sin[θ])/Sqrt[(Globalx - r Cos[θ])^2 + (v t - μ - r Sin[θ])^2],
   (NewGaus[(r Cos[θ])^2 + (r Sin[θ])^2, σ, mn] r)/Sqrt[(Globalx - r Cos[θ])^2 + (v t - μ - r Sin[θ])^2] Sin[ArcCos[(v t - μ - r Sin[θ])/Sqrt[(Globalx - r Cos[θ])^2 + (v t - μ - r Sin[θ])^2]]]},
  {r, 0, rc}, {θ, 0, 2 π}]
Globalx = 0;
ExtendedHphiVer2XAndYCom[t_, μy_, σ_, mn_, yp_, rc_, μx_] :=
 1/(2 π) NIntegrate[{(NewGaus[(r Cos[θ])^2 + (r Sin[θ])^2, σ, mn] r)/Sqrt[(Globalx - μx - r Cos[θ])^2 + (v t - μy - r Sin[θ])^2] (v t - μy - r Sin[θ])/Sqrt[(Globalx - μx - r Cos[θ])^2 + (v t - μy - r Sin[θ])^2],
   (NewGaus[(r Cos[θ])^2 + (r Sin[θ])^2, σ, mn] r)/Sqrt[(Globalx - μx - r Cos[θ])^2 + (v t - μy - r Sin[θ])^2] Sin[ArcCos[(v t - μy - r Sin[θ])/Sqrt[(Globalx - μx - r Cos[θ])^2 + (v t - μy - r Sin[θ])^2]]]}, {r, 0, rc}, {θ, 0, 2 π}]
OffSetFiber = 0;
OLDxxxResultMatrix = xxxResultMatrix;
OLDResultMatrix = ResultMatrix;
NrTube = 2;
AllNewModelH[x_] :=
 Sum_{i=1}^{TubeCount} NewModelH[x - BigN[[i, 2]], JSDev[[i]], JMean[[i]] BinJ[[i]], r[[i]]]
AllVecFNewModelH[x_, y_] :=
 Sum_{i=1}^{TubeCount} NewModelH[Sqrt[(x - BigN[[i, 2]])^2 + y^2], JSDev[[i]], JMean[[i]] BinJ[[i]],
   r[[i]]] {-Sin[ArcTan[x - BigN[[i, 2]], y]], Cos[ArcTan[x - BigN[[i, 2]], y]]}
AdvancedAllVecFNewModelH[x_, y_] :=
 Sum_{i=1}^{TotalPipes} NewModelH[Sqrt[(x - BigN[[i, 2]])^2 + (y - AlongY[[i]])^2], JSDev[[i]],
   JMean[[i]] BinJ[[i]], r[[i]]] {-Sin[ArcTan[x - BigN[[i, 2]], y - AlongY[[i]]]],
   Cos[ArcTan[x - BigN[[i, 2]], y - AlongY[[i]]]]}
TotalNewModelH[x_, y_] :=
 Sum_{i=1}^{TotalPipes} NewModelH[Sqrt[(x - BigN[[i, 2]])^2 + (y - AlongY[[i]])^2],
  JSDev[[i]], JMean[[i]] BinJ[[i]], r[[i]]]
```

Appendix D

This appendix and appendix C gives the *Mathematica* code for the implementation of the method 2 magnetic field calculation.

```
Gaus[x_, μ_, σ_, mn_] := mn Exp[-(x - μ)^2 / (2 σ^2)]
NewGaus[x_, σ_, mn_] := mn Exp[-(x) / (2 σ^2)]
Globalx = 0;
ExtendedHphiVer2XAndYCom[t_, μy_, σ_, mn_, yp_, rc_, μx_] :=
  1/(2 π) NIntegrate[ { NewGaus[(r Cos[θ])^2 + (r Sin[θ])^2, σ, mn] r / Sqrt[(Globalx - μx - r Cos[θ])^2 + (v t - μy - r Sin[θ])^2] * (v t - μy - r Sin[θ]) / Sqrt[(Globalx - μx - r Cos[θ])^2 + (v t - μy - r Sin[θ])^2],
     NewGaus[(r Cos[θ])^2 + (r Sin[θ])^2, σ, mn] r / Sqrt[(Globalx - μx - r Cos[θ])^2 + (v t - μy - r Sin[θ])^2] * (Globalx - μx - r Cos[θ]) / Sqrt[(Globalx - μx - r Cos[θ])^2 + (v t - μy - r Sin[θ])^2] },
    {r, 0, rc}, {θ, 0, 2 π}]
RMtxv2 = Array[rmte, {NN, 2}];
xxxRMtxv2 = Array[xxxrmte, {NN, 2}];
temp = {0, 0};

For[i = 1, i <= NN, i++, t = i Δt;
 RMtxv2[[i, 1]] = t; x = v t; For[j = 1, j <= TotalPipes, j++,
  temp = ExtendedHphiVer2XAndYCom[t, BigN[[j, 2]], JSDev[[j]], JMean[[j]] BinJ[[j]],
      BigN[[j, 2]] - x, r[[j]], AlongY[[j]]] + temp;];
 RMtxv2[[i, 2]] = temp; Print["Counter: ", i, "  temp: ", temp];
    temp = {0, 0};]
```

DANISH METEOROLOGICAL INSTITUTE

Scientific Reports

Scientific reports from the Danish Meteorological Institute cover a variety of geophysical fields, i.e. meteorology (including climatology), oceanography, subjects on air and sea pollution, geomagnetism, solar-terrestrial physics, and physics of the middle and upper atmosphere.

Reports in the series within the last five years:

No. 94-1
Bjørn M. Knudsen: Dynamical processes in the ozone layer

No. 94-2
J. K. Olesen and K. E. Jacobsen: On the atmospheric jet stream with clear air turbulences (CAT) and the possible relationship to other phenomena including HF radar echoes, electric fields and radio noise

No. 94-3
Ole Bøssing Christensen and Bent Hansen Sass:
A description of the DMI evaporation forecast project

No. 94-4
I.S. Mikkelsen, B. Knudsen, E. Kyrö and M. Rummukainen: tropospheric ozone over Finland and Greenland, 1988-94
Not published

No. 94-5
Jens Hesselbjerg Christensen, Eigil Kaas, Leif Laursen: The contribution of the Danish Meteorological Institute (DMI) to the EPOCH project "The climate of the 21st century" No. EPOC-003-C (MB)

No. 95-1
Peter Stauning and T.J. Rosenberg:
High-Latitude, day-time absorption spike events
1. morphology and occurrence statistics
Not published

No. 95-2
Niels Larsen: Modelling of changes in stratospheric ozone and other trace gases due to the emission changes : CEC Environment Program Contract No. EV5V-CT92-0079. Contribution to the final report

No. 95-3
Niels Larsen, Bjørn Knudsen, Paul Eriksen, Ib Steen Mikkelsen, Signe Bech Andersen and Torben Stockflet Jørgensen: Investigations of ozone, aerosols, and clouds in the arctic stratosphere : CEC Environment Program Contract No. EV5V-CT92-0074. Contribution to the final report

No. 95-4
Per Høeg and Stig Syndergaard: Study of the derivation of atmospheric properties using radio-occultation technique

No. 95-5
Xiao-Ding Yu, **Xiang-Yu Huang** and **Leif Laursen** and Erik Rasmussen: Application of the HIRLAM system in China: heavy rain forecast experiments in Yangtze River Region

No. 95-6
Bent Hansen Sass: A numerical forecasting system for the prediction of slippery roads

No. 95-7
Per Høeg: Proceeding of URSI International Conference, Working Group AFG1 Copenhagen, June 1995. Atmospheric research and applications using observations based on the GPS/GLONASS System
Not published

No. 95-8
Julie D. Pietrzak: A comparison of advection schemes for ocean modelling

No. 96-1
Poul Frich (co-ordinator), H. Alexandersson, J. Ashcroft, B. Dahlström, G.R. Demarée, A. Drebs, A.F.V. van Engelen, E.J. Førland, I. Hanssen-Bauer, R. Heino, T. Jónsson, K. Jonasson, L. Keegan, P.Ø. Nordli, **T. Schmith**, **P. Steffensen**, H. Tuomenvirta, O.E. Tveito: North Atlantic Climatological Dataset (NACD Version 1) - Final report

No. 96-2
Georg Kjærgaard Andreasen: Daily response of high-latitude current systems to solar wind variations: application of robust multiple

regression. Methods on Godhavn magnetometer data

No. 96-3
Jacob Woge Nielsen, Karsten Bolding Kristensen, Lonny Hansen: Extreme sea level highs: a statistical tide gauge data study

No. 96-4
Jens Hesselbjerg Christensen, Ole Bøssing Christensen, Philippe Lopez, Erik van Meijgaard, Michael Botzet: The HIRLAM4 Regional Atmospheric Climate Model

No. 96-5
Xiang-Yu Huang: Horizontal diffusion and filtering in a mesoscale numerical weather prediction model

No. 96-6
Henrik Svensmark and Eigil Friis-Christensen:
Variation of cosmic ray flux and global cloud coverage - a missing link in solar-climate relationships

No. 96-7
Jens Havskov Sørensen and Christian Ødum Jensen: A computer system for the management of epidemiological data and prediction of risk and economic consequences during outbreaks of foot-and-mouth disease. CEC AIR Programme. Contract No. AIR3 - CT92-0652

No. 96-8
Jens Havskov Sørensen: Quasi-automatic of input for LINCOM and RIMPUFF, and output conversion. CEC AIR Programme. Contract No. AIR3 - CT92-0652

No. 96-9
Rashpal S. Gill and Hans H. Valeur:
Evaluation of the radarsat imagery for the operational mapping of sea ice around Greenland

No. 96-10
Jens Hesselbjerg Christensen, Bennert Machenhauer, Richard G. Jones, Christoph Schär, Paolo Michele Ruti, Manuel Castro and Guido Visconti:
Validation of present-day regional climate simulations over Europe: LAM simulations with observed boundary conditions

No. 96-11
Niels Larsen, Bjørn Knudsen, Paul Eriksen, Ib Steen Mikkelsen, Signe Bech Andersen and Torben Stockflet Jørgensen: European Stratospheric Monitoring Stations in the Artic: An European contribution to the Network for Detection of Stratospheric Change (NDSC): CEC Environment Programme Contract EV5V-CT93-0333: DMI contribution to the final report

No. 96-12
Niels Larsen: Effects of heterogeneous chemistry on the composition of the stratosphere: CEC Environment Programme Contract EV5V-CT93-0349: DMI contribution to the final report

No. 97-1
E. Friis Christensen og C. Skøtt: Contributions from the International Science Team. The Ørsted Mission - a pre-launch compendium

No. 97-2
Alix Rasmussen, Sissi Kiilsholm, Jens Havskov Sørensen, Ib Steen Mikkelsen: Analysis of tropospheric ozone measurements in Greenland: Contract No. EV5V-CT93-0318 (DG 12 DTEE): DMI's contribution to CEC Final Report Arctic Trophospheric Ozone Chemistry ARCTOC

No. 97-3
Peter Thejll: A search for effects of external events on terrestrial atmospheric pressure: cosmic rays

No. 97-4
Peter Thejll: A search for effects of external events on terrestrial atmospheric pressure: sector boundary crossings

No. 97-5
Knud Lassen: Twentieth century retreat of sea-ice in the Greenland Sea

No. 98-1
Niels Woetman Nielsen, Bjarne Amstrup, Jess U. Jørgensen:
HIRLAM 2.5 parallel tests at DMI: sensitivity to type of schemes for turbulence, moist processes and advection

No. 98-2
Per Høeg, Georg Bergeton Larsen, Hans-Henrik Benzon, Stig Syndergaard, Mette Dahl Mortensen: The GPSOS project
Algorithm functional design and analysis of ionosphere, stratosphere and troposphere observations

No. 98-3
Mette Dahl Mortensen, Per Høeg:
Satellite atmosphere profiling retrieval in a nonlinear troposphere
Previously entitled: Limitations induced by Multipath

No. 98-4
Mette Dahl Mortensen, Per Høeg:

Resolution properties in atmospheric profiling with GPS

No. 98-5
R.S. Gill and M. K. Rosengren
Evaluation of the Radarsat imagery for the operational mapping of sea ice around Greenland in 1997

No. 98-6
R.S. Gill, H.H. Valeur, P. Nielsen and K.Q. Hansen: Using ERS SAR images in the operational mapping of sea ice in the Greenland waters: final report for ESA-ESRIN's: pilot projekt no. PP2.PP2.DK2 and 2nd announcement of opportunity for the exploitation of ERS data projekt No. AO2..DK 102
Not published

No. 98-7
Per Høeg et al.: GPS Atmosphere profiling methods and error assessments

No. 98-8
H. Svensmark, N. Woetmann Nielsen and A.M. Sempreviva: Large scale soft and hard turbulent states of the atmosphere

No. 98-9
Philippe Lopez, Eigil Kaas and Annette Guldberg: The full particle-in-cell advection scheme in spherical geometry

No. 98-10
H. Svensmark: Influence of cosmic rays on earth's climate

No. 98-11
Peter Thejll and Henrik Svensmark: Notes on the method of normalized multivariate regression

No. 98-12
K. Lassen: Extent of sea ice in the Greenland Sea 1877-1997: an extension of DMI Scientific Report 97-5

No. 98-13
Niels Larsen, Alberto Adriani and Guido DiDonfrancesco: Microphysical analysis of polar stratospheric clouds observed by lidar at McMurdo, Antarctica

No.98-14
Mette Dahl Mortensen: The back-propagation method for inversion of radio occultation data

No. 98-15
Xiang-Yu Huang: Variational analysis using spatial filters

No. 99-1
Henrik Feddersen: Project on prediction of climate variations on seasonel to interannual timescales (PROVOST) EU contract ENVA4-CT95-0109: DMI contribution to the final report:Statistical analysis and post-processing of uncoupled PROVOST simulations

No. 99-2
Wilhelm May: A time-slice experiment with the ECHAM4 A-GCM at high resolution: the experimental design and the assessment of climate as compared to a greenhouse gas experiment with ECHAM4/OPYC at low resolution

No. 99-3
Niels Larsen et al.: European stratospheric monitoring stations in the Artic II: CEC Environment and Climate Programme Contract ENV4-CT95-0136. DMI Contributions to the project

No. 99-4
Alexander Baklanov: Parameterisation of the deposition processes and radioactive decay: a review and some preliminary results with the DERMA model

No. 99-5
Mette Dahl Mortensen: Non-Linear High Resolution Inversion of Radio Occultation Data

No. 99-6
Stig Syndergaard: Retrieval analysis and methodologies in atmospheric limb sounding using the GNSS radio occultation technique

No. 99-7
Jun She, Jacob Woge Nielsen: Operational wave forecasts over the Baltic and North Sea

No. 99-8
Henrik Feddersen: Monthly temperature forecasts for Denmark - statistical or dynamical?

No. 99-9
P. Thejll, K. Lassen: Solar forcing of the Northern hemisphere air temperature: new data (In Press)

No. 99-10
Torben Stockflet Jørgensen, Aksel Walløe Hansen: Comment on "Variation of cosmic ray flux and global coverage - a missing link in solar-climate relationships" by Henrik Svensmark and Eigil Friis-Christensen

No. 99-11
Mette Dahl Meincke:
Inversion Methods for Atmospheric Profiling with GPS Occultations
(In Press)